Journal

NeuroImage

Review for Special Issue *Functional Near Infrared Spectroscopy (fNIRS)*, Guest Editors: David Boas, Clare Elwell, Marco Ferrari, Gentaro Taga

Title

Time domain functional NIRS imaging for human brain mapping

Author names and affiliations

Alessandro Torricelli[a*], Davide Contini[a], Antonio Pifferi[a], Matteo Caffini[b], Rebecca Re[a], Lucia Zucchelli[a], Lorenzo Spinelli[c]

[a] Politecnico di Milano – Dipartimento di Fisica, piazza Leonardo da Vinci 32, I-20133, Milan, Italy

[b] Politecnico di Milano – Dipartimento di Elettronica, Informazione e Bioingegneria, via Golgi 39, I-20133, Milan, Italy

[c] Istituto di Fotonica e Nanotecnologie, Consiglio Nazionale delle Ricerche, piazza Leonardo da Vinci 32, I-20133, Milan, Italy

Corresponding author

Alessandro Torricelli

Address: Politecnico di Milano - Dipartimento di Fisica, piazza Leonardo da Vinci, 32, I-20133 Milan, Italy

Telephone: +39 02 2399 6087

Fax: +39 02 2399 6126

Email: alessandro.torricelli@polimi.it

Abstract

This review is aimed at presenting the state-of-the-art of time domain (TD) functional near-infrared spectroscopy (fNIRS). We first introduce the physical principles, the basics of modeling and data analysis. Basic instrumentation components (light sources, detection techniques, and delivery and collection systems) of a TD fNIRS system are described. A survey of past, existing and next generation TD fNIRS systems used for research and clinical studies is presented. Performance assessment of TD fNIRS systems and standardization issues are also discussed. Main strengths and weakness of TD fNIRS are highlighted, also in comparison with continuous wave (CW) fNIRS. Issues like quantification of the hemodynamic response, penetration depth, depth selectivity, spatial resolution and contrast-to-noise ratio

are critically examined, with the help of experimental results performed on phantoms or *in vivo*. Finally we give an account on the technological developments that would pave the way for a broader use of TD fNIRS in the neuroimaging community.

Keywords

Functional near-infrared spectroscopy, Time domain, Continuous wave, Instrumentation, Penetration depth, Depth selectivity

Conflict of interest

The Authors have no relationships with the commercial companies cited in the paper that could inappropriately influence, or be perceived to influence, their work.

Abbreviations

AOTF, acousto-optic tunable filter

CNR, contrast-to-noise ratio

CW, continuous wave

DE, diffusion equation

DTOF, distribution of time-of-flight

FD, frequency domain

FEM, finite element method

fNIRS, functional near-infrared spectroscopy

FWHM, full width at half maximum

GI, graded index

ICCD, intensified charge coupled device

IEC, International Electrotechnical Commission

IRF, instrument response function

ISO, International Organization for Standardization

LDF, laser Doppler flowmetry

MCP, micro-channel plate

MPE, maximum permissible exposure

NA, numerical aperture

NIRS, near-infrared spectroscopy

OD, optical density

OTDR, optical time domain reflectometer

PMT, photomultiplier tube

RTE, radiative transfer equation

SC, supercontinuum

SI, step index

SPAD, single-photon avalanche diode

SRS, space-resolved spectroscopy

TCSPC, time-correlated single photon counting

TD, time domain

TPSF, temporal point spread function

Contents

Introduction

This review is aimed at presenting the state-of-the-art of time domain (TD) functional near-infrared spectroscopy (fNIRS). As described in a recent review on the history of fNIRS (Ferrari and Quaresima, 2012), while fNIRS dates back about 20 years ago, we have to wait till 1996 for the first single-channel TD fNIRS study to appear in the literature (Obrig et al., 1996), and only some years later, in 1998-2000, the first papers describing multi-channel TD fNIRS instruments were published (Hintz et al., 1998; Eda et al., 1999; Cubeddu et al., 1999; Ntziachristos et al., 1999; Oda et al., 1999; Schmidt et al., 2000).

Noticeably, from the physical and technological point of view the origin of TD fNIRS can be traced back to the 1980s, when researchers started exploring the fascinating field of diffusing photons in random (e.g. biological) media (Kuga et al., 1983). ~~F~~A few years later, several studies were focused on diffuse optical imaging and spectroscopy with pulsed laser and photo-detection techniques with picosecond resolution (Chance et al., 1988; Delpy et al., 1988; Ho et al., 1989; Jacques, 1989a; Jacques, 1989b; Patterson et al., 1989).

Nowadays, about thirty years after the first studies, there is only one dual-channel TD fNIRS commercial ~~(not sold outside of Japan)~~ system (Hamamatsu Photonics, 2013e) not sold outside of Japan, ~~-~~while there are no commercial TD fNIRS imagers available (Contini et al., 2012; Ferrari and Quaresima, 2012). A ~~F~~few laboratory prototypes have been developed by research groups located in academic or public research centers. To some extent this situation could be interpreted as the failure of the TD approach within ~~B~~biomedical o~~O~~ptics. Indeed, in part of the scientific community TD fNIRS (and TD techniques in general) has the reputation of being cumbersome, bulky, and very expensive as compared to commercial continuous wave (CW) fNIRS systems. At the time of writing we cannot ignore all these pitfalls and a gap still exists between CW and TD fNIRS technology. However, we are at the forefront of a new era where recent advances in photonic technologies might allow TD fNIRS to bridge the gap and potentially to overtake CW fNIRS. In this review we try to substantiate this foresight by outlining the key physical and technological ~~issues~~ aspects that will allow TD fNIRS to reach a maturity stage and to spread in the biomedical and neuroimaging community.

In the following sections we first describe the principles behind TD fNIRS and the basics of TD fNIRS instrumentation. We then highlight the main strengths and weaknesses of TD fNIRS, ~~also~~ notably in comparison with CW fNIRS. A concise survey of TD fNIRS data analysis and applications is further reported. Finally we ~~will~~ give an account on future perspectives and technological developments that pave the way for a broader use of TD fNIRS in the neuroimaging community.

Principles of TD fNIRS

Basics of NIRS

To properly understand the principles of TD fNIRS it is useful to briefly recall the basics of near-infrared spectroscopy (NIRS). NIRS is a powerful spectroscopic technique used in several fields (e.g. food and agriculture, chemical industry, life sciences, medical and pharmaceutical, textiles) to nondestructively test samples like liquids (e.g. in the food sector: oil, wine, and milk), powders (e.g. pharmaceutical tablets and pills, wheat flour, …), and bulk objects (e.g. in the food sector: fruits and vegetables, meat, cheese, …), allowing for their analytical and chemical characterization (Siesler et al., 2002).

In the biomedical field NIRS makes use of light to noninvasively monitor tissue hemodynamics and oxidative metabolism (Ferrari et al., 2012). In the 600-1000 nm spectral range, light attenuation by the main tissue constituents (i.e. water, lipid, and hemoglobin) is in fact relatively low and ~~accounts~~ allows for penetration through several centimeters of tissue. Moreover, the difference in the absorption spectra of oxygenated and deoxygenated hemoglobin allows the separate measurement~~s~~ of the concentration of these two species (O_2Hb and HHb, respectively), and the derivation of physiologically relevant parameters like total hemoglobin concentration (tHb = HHb + O_2Hb) and blood oxygen saturation (SO_2 = O_2Hb/tHb). The term fNIRS is then used to specifically address NIRS applications in the neuroimaging field aiming at mapping and understanding the functioning of the human brain cortex.

In NIRS a weak (a few mW) light signal is injected in the tissue and the ~~r~~emitted signal which carries information on tissue constituents is measured. As a result of the microscopic discontinuities in the refractive index of biological tissues, NIR light is highly scattered, therefore it is the complex interplay between light absorption and light scattering that determines the overall light attenuation. Proper physical models for photon migration (e.g. diffusion, random walk, Monte Carlo) should be used to correctly interpret NIRS signals unraveling the absorption from the diffusive contribution (Martelli et al., 2009; Durduran et al., 2010).

The feature physical quantities in a diffusive medium are the scattering length l_s and the absorption length l_a, representing the photon mean free path between successive scattering and absorption events, respectively. Equivalently, the scattering coefficient $\mu_s = 1/l_s$ and the absorption coefficient $\mu_a = 1/l_a$ (typically expressed in units of mm^{-1} or cm^{-1}) are used to indicate the scattering and the absorption probability per unit length, respectively. Due to anisotropy in light propagation, a reduced scattering coefficient is ~~typically~~ introduced $\mu_s' = \mu_s (1-g)$, where g is the anisotropy factor (Martelli et al., 2009).

Typically in a NIRS measurement, light is delivered to and collected from the sample by means of optical fibers (optodes) or other simple optical systems (e.g. relay lenses), which ~~results in ease of use~~simplify the use of the instrumentation, especially when dealing with clinical measurements on volunteers or patients. A f~~F~~ew commercial systems allow placing light sources and detectors directly in contact with the probed tissue. The simplest NIRS measurement configuration is the *transmittance* mode with the

injection and collection fibers on opposite surfaces. In the biomedical field this ~~can be rarely~~is only possible ~~like~~ for a few applications such as hemorrhage detection in newborns (Gibson et al., 2006), thanks to the small size and transparency of the head, ~~for~~ optical mammography, where the female breast is gently compressed by parallel transparent plates (Taroni et al., 2012), or ~~for~~ finger arthritis detection (Golovko et al., 2011), where the thinned shape of the finger makes this possible. On the other hand, the *reflectance* mode exploits the fact that, thanks to scattering, light is highly diffused in the sample volume and NIRS measurements become possible with a couple of optic fibers placed on the same surface of the tissue at a distance of a few centimeters. A combination of several injection and collection fibers on regularly spaced arrangements permits topography or tomographic approaches (~~Boas et. al.~~Selb et al., 2011).

Independently from the measurement geometry, three different NIRS approaches can be implemented: *i*) CW NIRS makes use of a steady state light source (e.g. a light emitting diode or a laser with intensity constant in time) that can be typically amplitude modulated at a low (a few kHz) frequency in order to exploit the significant improvements in sensitivity available from phase-locked detection techniques, and of a detection apparatus sensitive to light attenuation changes (e.g. photodiode); *ii*) Frequency domain (FD) NIRS is based on amplitude modulated light sources (at frequency of the order of 100MHz or larger, up to ~1 GHz) and on the detection of light amplitude demodulation and phase shift; *iii*) TD NIRS employs a pulsed light source, typically a laser providing light pulses with duration of a few tens of picoseconds, and a detection apparatus with temporal resolution in the sub-nanosecond scale. A detailed review of these different approaches can be found in Wolf et al. (2007).

The classical TD NIRS approach

TD NIRS relies on the ability to measure the photon distribution of time-of-flight (DTOF) in a diffusive medium (in the literature the DTOF is also called temporal point spread function, TPSF). Following the injection of ~~the~~ a light pulse within a turbid medium, the DTOF measured at a fixed distance from the injection point (typically in the range 10 – 40 mm) is delayed, broadened, and attenuated. The delay is a consequence of the finite time that light takes to travel the distance between the source and detector; broadening is mainly due to the different paths that photons undergo because of multiple scattering; attenuation appears because absorption reduces the probability of detecting a photon, and diffusion into other directions within the medium decreases the number of detected photons in the considered direction. Increasing the source-detector distance yields an increased delay and broadening of the DTOF and decreases the number of detected photons. Similar behavior is observed when the scattering increases. Finally, absorption affects both the signal intensity and the trailing edge (i.e. slope of the tail) of the DTOF, whilst leaving the temporal position of the DTOF substantially unchanged.

Fig. 1 shows the effect of source detector distance, absorption, and reduced scattering on TD NIRS signals in a homogeneous diffusive medium mimicking a biological tissue. While this is an oversimplification of the real geometry of a human head, nonetheless the model is useful to present the basics of TD NIRS. In the following section we will discuss the effect of tissue heterogeneity (e.g. the layered structure of the human head) on TD NIRS signals.

The null source detector distance TD NIRS approach

In 2005 a collaborative effort between the research groups at Politecnico di Milano, Milan, Italy, and at University of Florence, Italy, produced an innovative approach for the investigation of highly diffusive media, based on TD NIRS reflectance measurements at null source-detector separation (Torricelli et al., 2005). The null distance TD NIRS approach was to some extent ground-breaking, since the classical TD NIRS approach to diffuse imaging and spectroscopy fixed source and detector at a large distance to avoid the inaccurate description of light propagation based on photon diffusion at early time and short distance. A major misconception in TD NIRS is that penetration depth is dependent on source detector distance, like in CW NIRS. On the contrary,~~Indeed,~~ it was demonstrated by means of numerical simulations that the null distance approach yields better spatial resolution and contrast with respect to the use of longer source detector distances, for an absorbing point-like inclusion embedded in a homogeneous medium. The extension to absorption and scattering inclusions with finite dimensions and to layered geometries, better describing some biological structures, such as head or muscle, was reported (Spinelli et al., 2006).

TD fNIRS Modeling and Data Analysis

The raw data in TD fNIRS measurements consist of several time series of DTOFs, acquired at two or more wavelengths, typically from multiple locations. Each DTOF has to be processed to extract the relevant information. Values for the hemodynamic parameters in the brain cortex can be estimated from the corresponding values of the absorption coefficients by means of Beer's law. In a pioneer TD fNIRS study the absorption coefficient was estimated by simply fitting the tail of the measured TD NIRS signal with an exponential law (Chance et al., 1988; Nomura et al., 1997). Nowadays, to properly model light propagation in diffusive media in the TD regime, a wealth of analytical and numerical tools exists, for both simulation purposes (forward model) and for the interpretation of experimental results (inverse model).

Forward model

The diffusion equation (DE), an approximation to the radiative transfer equation (RTE) for the case of highly diffusive media, is the most commonly used framework in which photon migration has been treated. A fundamental paper for the TD NIRS approach was published in 1989 by Patterson, Chance and Wilson (Patterson et al., 1989) presenting the analytical solution of the DE for TD NIRS in a homogeneous semi-infinite medium or in an infinite slab. Since then, many other papers have been published with improved description of the boundary conditions (e.g. extrapolated or partial current boundary), with analytical solutions for different geometry (e.g. parallelepiped, sphere, cylinder) and for heterogeneous cases (e.g. layered medium, point-like perturbation). It is not the scope of this review paper to describe in details all these contributions. We simply mention for the interested reader that recently, Martelli et al. (2009) have collected in a comprehensive book the basic theory of photon migration together with analytical solutions for the DE in the CW and TD regime (also implemented in the Fortran programming language) for several geometries. Other handbooks similarly treat the same issues (Tuchin, 2010; ~~Boas~~ Hielscher et al., 2011).

Analytical solutions of the RTE have been recently provided for TD NIRS (Liemert and Kienle, 2012; Simon et al., 2013) aiming at overcoming the basics limitation of the DE (e.g. modeling photon migration at very short times or distances, with high absorption, or low scattering). Further, the analytical description of TD perturbation in a homogeneous diffusive medium has greatly improved, being able to deal not only with point-like weakly absorbing inclusions, but also with large highly absorbing objects (Sassaroli et al., 2010).

While to a first approximation the description of light propagation in realistic geometries (i.e. adult head) can be treated with simplified analytical models (e.g. layered or perturbed models), it is well known that the use of numerical methods can provide more flexible and accurate solutions. The finite element method (FEM) is a powerful numerical approach to provide solutions of the DE in any geometry and it has been used since 1993 in Biomedical Optics to model light propagation (Arridge et al., 1993). Nowadays freely available tools exist that implement FEM and also handle meshing of MRI anatomical data (TOAST, 2013; NIRFAST, 2013). The Monte Carlo method provides the most accurate description of light propagation in diffusive media (Wang et al., 1995; MCML, 2013), but in the past it was hindered by a very long computational time. Nonetheless it was used by several researchers to properly simulate photon migration in realistic adult and neonatal head models (Boas et al., 2002; Fukui et al., 2003). With the advent of parallelization on graphical processing units (Alerstam et al., 2008b; Fang and Boas, 2009; Ren et al., 2010), computational times have been reduced ~~of~~ by up to 100 times, and researchers have revived the use of Monte Carlo methods (Dehaes et al., 2011a; Sassaroli and Martelli, 2012). Recently, a further improvement in terms of speed, memory usage, and accuracy has been obtained by implementing a 3D code that represents a complex domain using a volumetric mesh (Fang, 2010, Fang and Kaeli, 2012).

Inverse model

The accuracy of non-linear fitting procedures based on the classical Levenberg-Marquardt approach in conjunction with TD NIRS analytical models has been validated several times (Cubeddu et al., 1996; Alerstam et al., 2008a; Spinelli et al., 2009a). Recently, improved fitting procedures based either on the Bayesian approach, also known as optimal estimation (Martelli et al., 2012), or on genetic algorithms (Hieslcher et al., 2000; Zhao et al., 2010) haves been proposed. Regularization methods for diffuse optical tomography, largely adopted for processing CW data, have proved to be effective for TD NIRS data (Arridge, 1999; Gao et al., 2004; Selb et al., 2007), as also shown in other fields like optical mammography (Intes, 2005; Enfield et al., 2007) and molecular imaging of small animals (Lapointe et al., 2012; Advanced Research Technologies, 2013).

Semi-empirical approaches

Semi-empirical phenomenological approaches have been developed aiming at finding quantities derived from measured DTOF that exhibit high sensitivity to deep (cerebral) absorption changes and low sensitivity to superficial (systemic) absorption changes. Two main approaches have been pursued: the first involves the calculation of the moments of the DTOF, focusing in particular on the second order moment (i.e. variance) (Liebert et al., 2004, Liebert et al., 2012), or on higher order moments (Hervé et al., 2012); an alternative approach exploits time gating of the DTOF to separate late (deep) and early (superficial) photons (Selb et al., 2005, Contini et al., 2007). The main advantage of these methods is that they do not rely on nonlinear fitting procedures, rather they are based on linear direct formulas, significantly increasing the contrast-to-noise ratio.

Fig.2 shows an experimental DTOF and the instrument response function (IRF) obtained by facing the injection and collection fiber. Moments of the DTOF and a The typical time windows used in the time-gating semi-empirical approach are also shown. Data were acquired by the system described in Contini et al., (2006).

TD fNIRS instrumentation

The values of the optical parameters of biological tissue (i.e. human head) in the visible and NIR spectral range (e.g. μ_a = 0.005-0.05 mm^{-1}; μ_s' = 0.5-2.5 mm^{-1}) (Torricelli et al., 2001), together with the values of source detector distances commonly used (10 – 30 mm), set the time scale of TD NIRS measurements in the range 0.1-10 ns, and fix the light attenuation level to about 8 optical density. Therefore, the crucial features in the designing of a TD fNIRS system are temporal resolution and sensitivity. It is therefore the

combination of a specific light source with a proper detection technique that determines the overall performances of a TD NIRS (and TD fNIRS) set-up. A further element that can influence the functioning of the TD NIRS set-up is the delivery and collection system used to bring light pulses to the measured sample and to collect the NIRS signal. We briefly illustrate the main aspects related to these building blocks~~. , and then we will~~before presenting the existing TD fNIRS systems.

Light sources

Current commercially available pulsed lasers produce short (10-100 ps) and ultra-short (10-100 fs) light pulses, with repetition frequency up to 100 MHz, and average power in the range of 1-1000 mW.

Solid state lasers (e.g. Ti: Sapphire) provide a powerful and flexible solution for laboratory set-ups (Coherent Inc., 2013; Newport Corporation, 2013). They can in fact offer average power of ~ <1 W, repetition rates < 100 MHz, and pulse duration ~~<~~ under 1 ps over a broad wavelength range (e.g. 750-850 nm). ~~There are~~They provide the advantages of wavelength tunability over 400 nm, and high output power enabling time-multiplexing of the source over multiple positions. Their use in clinical TD fNIRS devices is somehow limited, mainly due to a bulky case and to the long time (~~<~~ 10 s) required to switch between wavelengths.

Pulsed diode lasers are provided by several companies (Advanced Laser Diode Systems GmbH, 2013; Alphalas GmbH, 2013; Becker & Hickl GmbH, 2013a; Edinburgh Photonics, 2013; Hamamatsu Photonics, 2013d; PicoQuant GmbH, 2013b). They are compact and robust, and they typically come with sufficient average power (< 5 mW), narrow spectral bandwidth (< 10 nm) and pulse duration (< 500 ps). Several TD systems have adopted this type of light source (see Table 1 and Table 2). Indeed, to reach acceptable performances, there is always a trade-off between output power and pulse duration: due to the particular modulation strategy (gain switching), output power < 1 mW has to be selected to obtain pulse duration < 100 ps. Another drawback is a long warm-up time (in some cases > 60 min) needed to achieve pulse time stability in the picosecond range.

In the last years, a few companies (Fianium UK Ltd., 2013b; NKT Photonics A/S, 2013b) have delivered commercial high-power fiber lasers based on supercontinuum (SC) generation. These devices are ultra-broadband radiation sources with high spectral brightness and excellent beam quality. Typically, a total average power of <10 W is generated over a broad spectral range (e.g. 400-2000 nm), allowing average spectral power of 1 mW/nm. A series of optoelectronic accessories are used for automatic wavelength selection and power adjustment. Only preliminary TD fNIRS studies have been reported with these sources, yet they could potentially replace laser diodes in clinical systems. For this to happen, issues related to power stability (critical due to the nonlinear SC generation) and robustness (affected by the

durability of fusion and splicing in the photonic crystal fiber) have to be solved (e.g. by means of feedback loop and opto-mechanical solutions).

We have to notice that the laser power should be fixed to proper values in order to avoid possible damage or injury to the tissue. No maximum permissible exposure (MPE) value for the brain has been determined, however, the light intensity on the brain surface during fNIRS can be safely estimated to be only a few percent of the solar irradiation (Kiguchi et al., 2007). Despite the fact that these considerations were made for CW fNIRS, they hold also for TD fNIRS. According to the safety regulations (International Electrotechnical Commission, 2001) the criteria for the MPE assessment in the case of a repetitively pulsed or modulated lasers are: i) each single pulse of the train shall not exceed the MPE for a single laser pulse of the same duration; ii) the average exposure for a pulse train of duration T shall not exceed the MPE for a single pulse of duration T; iii) the average exposure for a pulse train shall not exceed the MPE for a single pulse multiplied by the correction factor $N^{-0.25}$ (where N is the total number of pulses impinging the tissue). The first criterion limits the energy of ~~the~~ a single pulse in order to avoid nonlinear effects that can damage the tissue~~,~~; in this case pulse duration and peak power are critical. The second ~~criterion and the~~ and third criteria~~on~~ limit the average exposure in which the key factor is the average power. Thus, in ~~the~~ cases in which ~~the~~ a single pulse ~~has~~ does not have~~not~~ sufficient energy to ~~determine~~ cause damage, and considering a repetition frequency of tens of MHz, the limiting factor is the average power of the laser, as for CW laser light.

Detection techniques

To detect weak and fast light signals, several detection techniques with temporal resolution in the range of 1-250 ps and sufficient sensitivity are available.

Non-linear optical-gating (by means of Kerr effect, parametric amplification, or non-linear up-conversion) can be used if time-gating of the optical signal in the sub-picosecond time scale is required (Wang et al., 1991; Tolguenec et al., 1997). Indeed this approach requires complex and bulky system set-ups that limit its use to the laboratory scale and in particular for those applications where extreme time resolution is really needed: in the biomedical field the molecular imaging of small animals by optical projection tomography (Bassi et al., 2010), or in the physics of matter field the characterization of photonic glasses (Toninelli et al., 2008). On the contrary, ~~I~~in fNIRS applications sub-picosecond time resolution is definitely not mandatory (see also next section *Temporal resolution*).

The streak camera is a detection apparatus with time resolution in the 1-10 ps range able to operate as multi-wavelength or multi-channel detector by exploiting its bi-dimensional design (Hamamatsu Photonics, 2013a). TD fNIRS experiments in small animals were recently reported with a streak camera apparatus (Vignal et al., 2008; Mottin et al., 2011), but no extension to human studies seems feasible due

to a very high cost (also compared to non-linear time gating) and an overall complexity that prevents the use by personnel without an adequate expertise in controlling of scientific instrumentation. Pioneer fNIRS studies were performed to determine the optical path-length in the adult and/or newborn head (Delpy et al., 1988; Wyatt et al., 1990; van der Zee et al., 1992; Ferrari et al., 1993). No further fNIRS studies on human have been reported to our knowledge.

The pioneer studies by Hintz et. al (1998) and Benaron et al. (2000) used a TD fNIRS system based on a modified optical time domain reflectometer (OTDR). This approach has been later abandoned because of poor performances.

The time-correlated single photon counting (TCSPC) technique (O'Connor and Phillips, 1984) has been extensively used for fluorescence lifetime measurements since the 1970s and later for TD NIRS measurements in diffusive media. In a TCSPC experiment, the temporal profile of the NIRS signal is not directly measured but is retrieved by repeatedly measuring the delay between the trigger of the injected laser pulse and the detection of a (diffusively) reemitted photon for a statistically significant number of photons. A detector with a fast (< 1 ns) and stable single electron response is required. A variety of such detectors are commercially available: photomultiplier tube (PMT) (Hamamatsu Photonics, K.K., 2013c), micro-channel plate (MCP) PMT (Hamamatsu Photonics, K.K., 2013b), hybrid detector (Becker & Hickl GmbH, 2013b; PicoQuant GmbH, 2013a), and single-photon avalanche diode (SPAD) (Excelitas Technologies Corp, 2013; ID Quantique, 2013; Micro Photon Devices, 2013a; PicoQuant GmbH, 2013e; SensL, 2013b). A key parameter in TCSPC is the count rate, i.e. the number of photons per second which can be processed (or simply counted) without exceeding the single photon statistics. In the 1980s light sources were characterized by low intensity and low repetition rate (<10 KHz), and TCSPC electronic circuit speed was also limited (the dead time after the detection of a photon was on the order of 10 μs). The consequence for TCSPC was a very low count rate (<10^4 photon/s), which resulted in long acquisition times (several minutes). Nowadays the speed of commercially available TCSPC modules is 1000 times faster than the classic TCSPC devices (e.g. the dead time is as low as 100 ns). In combination with a laser with repetition rate in the order of tens of MHz, a TCSPC module has potentially the capability of processing a few 10^6 photons/s. Further, multi-dimensional TCSPC allows the simultaneous recording of photons from a large number of detectors (Becker & Hickl GmbH, 2013d; PicoQuant GmbH, 2013d; SensL, 2013a). A complete and updated description of TCSPC systems and applications (including TD fNIRS) can be found in Becker (2005).

Detection of TD NIRS signal is also possible with a time-gated intensified charge coupled device (ICCD) camera. It basically consists of a photocathode, an MCP PMT, and a phosphor screen. High temporal resolution can be achieved by fast gating of the intensifier cathode of the ICCD camera (LaVision BioTec GmbH, 2013). Years ago the time resolution was limited to about 1 ns restricting the use of the time-

gated ICCD camera, while recently ultra-short gates (e.g. <100 ps) can be achieved by using smaller image tubes. Like TCSPC, a time-gated ICCD camera is characterized by sensitivity down to single photon detection. Like a streak camera, the time-gated ICCD system is a bi-dimensional device, thus potentially able to measure the spatial and temporal profile of the remitted light from a diffusive medium by acquiring different images synchronized for different time delays with respect to the injection of the laser pulse. Every image contains the spatial information at a certain time instant, while the successive values stored in the memory and referring to the same pixel determine the temporal distribution of the detected signal. TD NIRS setups based on a time-gated ICCD camera have been reported for optical imaging of diffusive phantoms (D'Andrea et al., 2003) or small animals (Niedre et al., 2006). Preliminary TD fNIRS studies have used the time-gated ICCD camera as multi-channel device in combination with optical fibers of different length allowing for simultaneous detection of several time-gates (Selb et al., 2005; Selb et al., 2006), or as an imaging device (Sawosz et al., 2010; Zhao et al., 2011).

Nowadays, TCSPC systems are more easily found in prototypes and instruments for TD fNIRS (see also next section *TD fNIRS systems*). Since there is no striking advantage of TCSPC over time-gated ICCD camera, the choice of the technique is rather determined by an overall balance between costs, complexity and performances in relation also to the specific applications.

When the TD null source detector distance approach is considered, several technological issues should be taken into account. The most severe obstacle is the presence of early photons. With decreasing source detector distance, early photons increase at a much faster pace than the late photons and saturate the detection electronics. This prevents the extraction of long-lived photons that carry information from deep structures. Thus, an efficient mechanism to gate, or at least to reduce, the early photons is needed to be able to exploit the advantages of this approach.

This modality is available for a MCP PMT by acting on its gain, for an ICCD camera by operating on the gain of the intensifier, and also for a streak camera by controlling the ramp voltage so as to sweep electrons corresponding to initial photons out of the active surface of the CCD detector. In practice, in all these devices, only the detection stage after the photocathode is altered. Therefore this solution is effective if the required extinction ratio is not severe, since initial photons still impinge onto the photocathode and extract electrons, causing damage to the active surface and increasing significantly the background noise. An attempt to obtain null distance TD NIRS with an ICCD based system has been reported (Sawosz et al., 2012).

A possible alternative ~~could be to~~is the use of a SPAD. A key difference of SPAD detectors with respect to other approaches is the possibility to enable the device above threshold very quickly. When the SPAD is disabled, the avalanche process cannot start, and most of the electron-hole pairs generated by the

incoming photons recombine within the active area in a few tens of ps. Thus, this device is not damaged by the burst of initial photons, and a strong rejection of early photons can be achieved.

The first demonstration of the null distance approach with a SPAD based system has been reported by the research group at Politecnico di Milano, Milan, Italy, (Pifferi et al., 2008).

Finally, we mention that a completely different method for measuring TD optical quantities has been proposed using pseudorandom bit sequences as light source and a cross-correlation scheme to retrieve the impulse response (Chen and Zhu, 2002; Chen and Zhu, 2003). While, the overall performances of this approach were not satisfactory, this is an interesting example of cross-contamination between different fields.

Delivery and collection system

Due to the limitations related to the size of TD NIRS light sources and detectors, it is typically required that the light pulses are delivered to the sample (e.g. the head) and conveyed to the detectors by some kind of optical system. The easiest, and most common way, is to couple light into optical fibers or bundles, which ~~that~~ has the additional advantage, from the point of view of safety, of electrically isolating the measurement site from the device.

Single mode optical fibers are characterized by small core diameter (<10 μm) and typically operate in a narrow spectral range (<100 nm) centered at a specific operating wavelength in the visible and NIR range.

Multimode optical fibers are built with core diameter of different sizes (10-1000 μm) and operate over a broad spectral range (from ultraviolet ~~to UV~~ to NIR). Attenuation, numerical aperture (NA), and dispersion are the main characteristics related to optical fibers that have to be considered when designing a TD fNIRS system.

Light attenuation in modern low hydroxyl ions fused silica optical fibers (used in long range data transmission) is below 10 dB/km, while plastic optical fibers (for short range data transmission) has higher attenuation (<100 dB/km) (Gowar, 1993). Attenuation is therefore negligible for fiber length in the order of 10 m, as used in fNIRS.

The NA is related to the maximum acceptance angle of an optical fiber and it influences the light gathering ability of the fiber (Gowar, 1993). To maximize collection efficiency in TD NIRS, high NA values (e.g. >0.3) and large core diameters (e.g. >500 μm) should be preferred for the collection fibers since the total power that can be collected from a diffusive sample by a fiber scales with the squares of the NA and of the radius. Multimode fibers have to be preferred to single mode fibers to optimize light transmission efficiency in the TD fNIRS system.

Dispersion is a crucial parameter for TD fNIRS since it broadens the light pulses travelling in the fiber. When using a narrow bandwidth source (e.g. laser), total dispersion is dominated by modal dispersion in a

Formatted: Font: Symbol

Formatted: Font: Symbol

Formatted: Font: Symbol

multimode fiber, while material (chromatic) dispersion can be dominant in a single mode fiber. Modal dispersion can be greatly reduced by a proper design of the refraction index profile of the optical fiber: graded index (GI) fibers should be preferred to step index (SI) fibers. Typical value of dispersion in GI fibers is 1 ps/m, while it increases to about 100 ps/m in SI fibers (Gowar, 1993).

The optimal solution to reduce pulse broadening and maximize light transmission for light delivery and collection would be a multimode GI optical fiber with the highest NA and the largest core diameter. Multimode GI optical fibers are typically fabricated with 50, 62.5 and 100 □m core diameter, therefore limiting their applications in TD fNIRS to light delivery. For maximizing TD signal collection from the tissue a fiber with a much larger diameter is required. Unavoidably, SI fibers have to be chosen, being commercially available with core diameter up to 3000 µm. ~~Indeed,~~Unfortunately, the bending radius of such large fibers is not negligible (e.g. >50 / >150 mm for momentary / long term bend of a 1000 µm core diameter fiber), resulting in a limited flexibility. For ease of use, especially in the clinical environment, fiber bundles, made by gathering hundreds of smaller flexible fibers, have to be preferred. Modal dispersion turns out to be a limiting factor since SI fibers are used (the use of GI fibers would not improve the performances due to waveguide dispersion effects). A trade-off between fiber bundle length and NA is required, typically obtained by limiting fiber bundle length to a couple of meters. The use of longer bundles determines an overall unacceptable temporal resolution, quantified by the full width at half maximum (FWHM) of the IRF. Values of the IRF larger than 1 ns compromise the accuracy of TD NIRS measurements (Liebert et al., 2003).

Additional components and devices are typically used in delivery and collection systems. Switches, splitters and galvo mirrors multiplex light pulses in different location of the sample (e.g. for mapping purposes). Variable neutral density attenuators are used to equalize the signals, while lenses help in focusing light to the detection systems. Band-pass filters prevent room light to interfere with the TD ~~NISR~~ NIRS signal, and help in collecting the fluorescence signal from endogenous or exogenous chromophores like indo-cyanine green (Gerega et al., 2012; Milej et al., 2012). The main effect of these ~~devices~~ components is the introduction of additional attenuation terms that could reduce the overall responsivity of the TD fNIRS set-up (Wabnitz et al., 2011), while ~~there is~~ they have a negligible effect on the IRF.

Formatted: Font: Symbol

Formatted: Font: Symbol

TD fNIRS systems

In this section we present a survey of traditional (Table 1), state-of-the-art (Table 2) and next generation (Table 3) TD fNIRS systems. With the term *traditional* we refer to TD fNIRS systems that, to our knowledge, have been now discontinued, or replaced by novel upgraded systems, or used for other

applications. It is worth noting that, most of these systems represented a breakthrough as compared to classical TD NIRS laboratory systems, typically based on bulky gas lasers and massive accessories. Indeed, they were compact at the level of being transportable out of the lab (see Fig.3). In most cases they were able to operate simultaneously at two or more wavelengths. Parallel acquisition of up to tens of channels was possible, opening the way to mapping experiments. Nonetheless, they were characterized by sub-optimal performances due to a reduced count rate (on average < 1 MHz) and to low average power (< 1 mW) of the light sources. In many cases they were used for static imaging with very long acquisition times (up to several minutes), or for monitoring hemodynamic changes in a few channels with a relatively short acquisition time (< 1 s).

We consider then the *state-of-the-art* TD fNIRS systems that in the last five years (2008-2012) have been used for research and clinical fNIRS studies in adults and neonates, as reported in the literature.

Finally we report on the *next generation* TD systems to present the work that, to our knowledge, researchers are carrying out to test novel approaches and to implement advanced technological solutions aiming at improving performances of TD fNIRS devices. These set-ups have only provided proof of principle results, while no clinical studies have been reported.

We conclude this section reporting on the issues related to multimodality co-registration of TD fNIRS with other techniques and to performance assessment and standardization of TD fNIRS system.

Traditional TD fNIRS systems

A collaborative effort among t~~T~~he research groups ~~of Britton Chance~~ at the Department of Physics, Department of Bioengineering, and Department of Biochemistry/Biophysics at University of Pennsylvania, under the coordination of prof. Britton Chance, developed a multi-channel TD instrument (Ntziachristos et al., 1999). Spatially resolved measurements of contralateral primary motor-cortex activation during voluntary finger tapping were performed and successfully coregistered with fMRI data. ~~In an early work (Ntziachristos et al., 1999) the presented the instrument development and preliminary measurements on one adult volunteer in coregistration with fMRI. Absorption changes due to motor stimulation with voluntary finger tapping were monitored in the contralateral primary motor cortex area.~~ Results demonstrated the efficiency of the device in the detection of local optical variations as well as its good performances in coregistration with fMRI.

The TD fNIRS system developed at Stanford University, Palo Alto, California, was characterized by a ~~huge~~ large number of channels (34x34), allowing for the first diffuse optical tomography measurements, but it suffered for very low sensitivity. The acquisition times were tremendously long and applications were limited to static imaging of hemorrhage in newborns (Benaron et al., 2000).

The tomographic TD fNIRS system developed by the research group at the Department of Medical Physics and Bioengineering, University College London, overcame most of the limitations of the previous system, and it was successfully used not only for quasi static imaging in diseased newborns (Hebden et al., 2004; Austin et al., 2006) but also for functional studies in healthy newborns (Gibson et al., 2006).
After a preliminary TD fNIRS study with a laboratory set-up (Obrig et al., 1996), the research group at Physikalisch-Technische Bundesanstalt in Berlin, Germany, developed a compact system that was used for very relevant studies in which it was first demonstrated the ability of the TD approach to discriminate intra-cerebral and extra-cerebral contribution (Steinbrink et al., 2001; Liebert et al., 2004).
The compact 8-channel TD fNIRS system developed at Politecnico di Milano, Milan, Italy was used for studying the bilateral prefrontal cortex hemodynamic response to a verbal fluency task (Quaresima et al., 2005).
The research group in Strasbourg used an eight-channel system based on picosecond laser sources and a multi-anode MCP PMT to perform a single point measurement during a finger tapping experiment (Montcel et al., 2005; Montcel et al., 2006). An upgraded version of this system is now being used for molecular imaging of small animals (Montcel and Poulet, 2006).
Several studies on piglets (Ijichi et al., 2005a), infants (Ijichi et al., 2005b; Ijichi et al., 2005c) and adult (Hoshi et al., 2006, Ohmae et al., 2006; Ohmae et al., 2007; Sato et al., 2007; Yokose et al., 2010; Kakihana et al., 2010; Kakihana et al., 2012) have been reported with the commercial TD fNIRS instrument TRS-10 developed by Hamamatsu Photonics. Fewer studies were performed with the modified multi-channel set-up (Oda et al., 1999; Ueda et al., 2005).
The research group at the Massachusetts General Hospital, Athinoula A. Martinos Center, Charlestown, Massachusetts, developed a TD fNIRS system based on an ICCD detector coupled to 18 optical fibers of 7 different lengths creating an optical delay, and enabling simultaneous detection in 7 windows by step of 500 ps. P~~A p~~reliminary single wavelength result~~s~~ on ~~an~~ adult~~s~~ performing a motor task ~~was~~ were reported (Selb et al., 2005; Selb et al., 2006).

State-of-the-art TD fNIRS systems

Nowadays, there is only one commercial TD fNIRS system, the TRS-20 developed in Japan by Hamamatsu Photonics and sold (only in Japan) as an investigational-use only, stand-alone two-channel system. The TRS-20 employs thermo-electrically controlled picosecond laser diodes, operating at 760 nm, 800 nm, and 830 nm, with an overall temporal resolution <150 ps (IRF FWHM), and proprietary fast photomultipliers and TCSPC module (Oda et al., 2009; Hamamatsu Photonics, 2013e).

Existing TD fNIRS systems with clinical applications have been mainly developed by European research groups located in academic or public research centers~~, while researcher in US and Japan seem to be less involved~~.

The research group at Physikalisch-Technische Bundesanstalt, Berlin, Germany, has developed a three-wavelength four-detection-channel TCSPC instrument (Wabnitz et al., 2005; Wabnitz et al., 2010) that has been effectively used for bedside assessment of cerebral perfusion in stroke patients (Liebert et al., 2005; Steinkellner et al., 2010), to explore neurovascular coupling in combination with magneto-encephalography (Sander et al., 2007; Mackert et al., 2008) and to study systemic artifacts in TD fNIRS (Kirilina et al., 2012). With little modifications in the light sources and in the detectors, the system has been also used for fluorescence detection from exogenous chromophores in the adult human brain (Liebert et al., 2006; Jelzow et al., 2012).

In Warsaw, Poland, a 32-channel configuration has been assembled by doubling the switching and detection elements at the Institute of Biocybernetics and Biomedical Engineering (Kacprzak et al., 2007) and used in clinical applications ~~like~~ such as brain oxygenation measurements during carotid endartectomy (Kacprzak et al., 2012) and detection of brain traumatic lesions (Liebert et al., 2011).

A 16-source and 16-detector TD fNIRS imager with fast acquisition time (>5 ms per channel) was developed at Politecnico di Milano, Milan, Italy (Contini et al., 2006; Contini et al., 2009) and used to map the cortical response in healthy volunteers during cognitive studies (Butti et al., 2009; Molteni et al., 2012) and in epileptic patients with movement disorders during motor tasks (Torricelli et al., 2011). The same group developed a 2-source and 2-detector TD fNIRS system based on the space-multiplexing approach (Re et al., 2010) with improved sensitivity that was used to investigate the sensitivity of TD fNIRS to cortical and superficial systemic response (Aletti et al., 2012).

Finally, we mention that a couple of European companies sell components (pulsed lasers, photo-detectors and TCSPC modules) and stand-alone TD systems, with up to 4 channels, mainly for standard fluorescence lifetime applications, single molecule spectroscopy, and lifetime imaging with scanning microscopes (Becker & Hickl GmbH, 2013c; PicoQuant GmbH, 2013d). These products could be properly adapted to be used for investigational TD fNIRS studies (Diop et al., 2010).

Next generation TD fNIRS systems

The research group at the Department of Medical Physics and Bioengineering, University College London, designed and developed an upgraded version of the tomographic TD fNIRS system (MONSTIR 2). Main improvements with respect to the previous device are the use of a SC fiber laser equipped with an acousto-optic tunable filter (AOTF) device allowing a multi-wavelength approach, and the use of

modern TCSPC acquisition boards to replace the obsolete electronic modules. The system has been tested on preliminary measurements on newborns (Hebden, 2012a; Hebden et al., 2012b).

The ICCD based TD fNIRS system developed at the Massachusetts General Hospital, Athinoula A. Martinos Center, Charlestown, Massachusetts, has been recently upgraded by introducing a SC fiber laser to replace the Ti:Sapphire laser, and a set of band-pass filters on a fast filter wheel ~~an AOTF~~ to properly and rapidly select the operating wavelengths (Selb and Boas, 2012; Selb et al., 2013). The main limitation of the previous set-up (i.e. the operation at a single wavelength) has been therefore overcome.

A novel TD fNIRS system has been recently developed by researchers at Politecnico di Milano, Milan, Italy. The use of hybrid PMT with reduced afterpulsing allows acquisition of TD fNIRS signals over a larger dynamic and temporal range. Further, the space-multiplexing approach implemented by means of a cascade of fast fiber optic switches that sequentially delivers the different wavelengths in different injection channels, eliminates the cross-talk between TD NIRS signal at different wavelengths (Contini et al., 2013b).

The research group at Physikalisch-Technische Bundesanstalt, Berlin, Germany has been testing novel approaches for light delivery and collection. A cascade of splitters is used to illuminate in parallel several injection points to potentially reduce power loss. Time-multiplexing of TD NIRS signal from different channels allows parallel detections. Moreover, advanced PMT with improved sensitivity in the NIR (e.g. GaAs surface) or reduced after-pulsing (e.g. hybrid PMT) have been tested (Steinkellner et al., 2012).

In a different set-up, a novel non-contact system is used that utilizes a quasi-null source detector separation approach for TD NIRS, taking advantage of polarization-sensitive detection and a state-of-the-art fast-gated SPAD to detect late photons only, bearing information about deeper layers of the biological tissue. Measurements on phantoms and preliminary *in vivo* tests demonstrate the feasibility of the non-contact approach for the detection of optically absorbing perturbations buried up to a few centimeters beneath the surface of a tissue--like turbid medium (Mazurenka et al., 2012, Mazurenka et al., 2013).

On the basis of the experience gained with advanced laboratory setups (Pifferi et al., 2008; Tosi et al., 2011), a next generation TD fNIRS prototype implementing the null distance approach has been recently designed and developed at Politecnico di Milano, Milan, Italy. The instrument is based on a custom developed SC fiber laser (Fianium Ltd., Southampton, United Kingdom), providing two independent outputs at 710 nm and 820 nm, with a repetition frequency of 40 MHz, 100 mW average power at each wavelength, and a FWHM of < 50 ps. A fast-gating (< 500 ps) front-end electronics and two SPAD detectors are used to simultaneously acquire photons at different time-windows. Preliminary *in vivo* results show, for the first time, the possibility to non-invasively monitor cortical O_2Hb and HHb changes during a motor task with a source detector distance of < 5 mm (Contini et al., 2013a).

The collaboration between Ecole Polytechnique Federale de Lausanne and University Hospital Zurich, Switzerland, allowed researchers to design a 3D imager based on SPAD imager with 128x128 pixels capable of performing TD NIRS measurements with a resolution of <100 ps. The system is equipped with picosecond pulsed diode laser and a telecentric objective for non-contact measurements. The main drawback is at present the long time required to the readout circuitry to process the data. (Mata Pavia et al., 2011a; Mata Pavia et al., 2011b; Mata Pavia et al., 2012).

Co-registration with other modalities

There are no fundamental limitations that prevent the possibility to co-register ~~TD~~ fNIRS with other neuroimaging modalities. Multimodality should be pursued aiming not only at validating ~~TD~~ fNIRS, but also at better understanding the physiological processes following brain stimulation (Yucel et al., 2012) and at the minimization of physiological noise (Cooper et al., 2012b).

For instance TD fNIRS and electroencephalography (EEG) co-registration has been performed both for validating the TD fNIRS (Torricelli et al., 2011) and for the study of the neurovascular coupling (Jelzow et al., 2010; Bari et al., 2012). Experiments have been performed with ~~both~~ pre-mounted EEG caps ~~(Jelzow et al., 2010) and~~ or mounting of individual electrodes ~~(Torricelli et al., 2011; Bari et al., 2012)~~. In both cases no interferences have been reported, verifying that these neuroimaging techniques can be easily applied and co-applied. Moreover results of the different techniques showed agreement between them and with literature. ~~.~~ In neurovascular coupling studies, fNIRS allowed a reliable measure of oxy- and deoxyhemoglobin changes, permitting the identification of a cascade of responses and the quantification of temporal delays between electrical and vascular response~~s~~.

To co-register TD fNIRS and functional magnetic resonance imaging (fMRI), the TD fNIRS instrument should reside and be operated at a safe distance from the fMRI scanner. Therefore, the use of long (e.g. 10 m) optical fibers for light delivery and collection from the head of the subject is required. As discussed, temporal dispersion in the optical fibers introduces a degradation of the overall performance of the TD fNIRS system. A reduction of the NA (e.g. by spatial filtering the mode propagating in the outer part of the fiber bundle) is useful to maintaining the IRF at acceptable FWHM values. This comes unavoidably at the cost of a large loss of signal that has to be compensated by the use of very sensitive detectors (Brühl et al., 2005; Torricelli et al., 2007, Jelzow et al., 2009). Further, to fit the limited space between the head and the MRI cage, 90° bended optodes or prisms were used. The MR-compatible fNIRS systems were successfully employed. The combination of the two modalities introduced advantages for both sides: the analysis of optical data was validated and improved by using MR results as prior knowledge, while the calibration of the fMRI-BOLD signal could benefit from the fNIRS measured parameters.

Similarly, in TD fNIRS and magneto-encephalography (MEG) co-registration the use of 4.5 m long optical fiber bundles, mounted tangentially to the subject's head via prisms, has been reported since the instrument was positioned outside the magnetically shielded room. A modulation-based DC-MEG technique was used with the bed sinusoidally moved in a horizontal direction by a hydraulic piston. Only minor movement amplitudes of the head of a few millimeters were observed during the stimulation periods. (Sander et al., 2007; Mackert et al., 2008). In the reported papers, experiments were performed in MEG/TD fNIRS coregistration to characterize the dynamic of and the interaction between the cortical neuronal and vascular responses, i.e. the neurovascular coupling. The combined analysis provided not only a qualitative, but also a quantitative assessment of the temporal behaviors. Furthermore, the depth resolution of TD fNIRS enabled the separation of systemic and cerebral hemoglobin concentration changes. This eliminated the uncertainty of previous MEG/CW fNIRS recordings, where signal contaminations by extra-cerebral variations could not be excluded definitely.

Simultaneous co-registration of TD fNIRS and positron emission tomography (PET) were performed and no particular technical issues were raised (Ohmae et al., 2006). A good correlation coefficient was obtained between TD fNIRS-derived cerebral blood volume (CBV) and PET-derived CBV, while the absolute CBV levels by TD fNIRS were lower than those by PET The TD fNIRS technique combined with PET was employed to validate its good performances in the quantification of the hemoglobin concentration in the tissues. It was thus confirmed as a noninvasive and easy method to evaluate cerebral hemodynamics, and indicated as a highly valuable indicator for diagnosis and treatment of various diseases.

TD fNIRS signals from cortical regions and changes in micro-circulatory blood flow dynamics in the scalp as measured by laser Doppler flowmetry (LDF) were simultaneously recorded in a couple of recent studies (Aletti et al., 2012; Kirilina et al., 2012), strengthening that the model-based separation of time-resolved TD fNIRS early (superficial) and late (deep) photons is able to cancel, or at least attenuate, the surface confounding effects. Since LDF employs CW light sources, proper solutions (e.g. use of filters, offset positioning of the probes, time-multiplexing of the techniques) are required to avoid interference on TD fNIRS signals. Same cautions should also be used if when TD fNIRS is simultaneously co-registered with another optical technique like such as diffuse correlation spectroscopy (Diop et al., 2011; Busch et al., 2012).

Performance assessment and standardization

The compelling need for standardization and quality assessment of diffuse optics instruments is as a key requirement for the translation of new optical tools to effective clinical use (Hwang et al., 2012). The definition of common procedures for the performance assessment of instruments, implemented over a set

of highly calibrated and reproducible phantoms is a key requirement for the grading of system performances, the quantitative assessment of instrument upgrades, the validation of clinical prototypes, the enforcement of quality control and consistency in clinical studies, the comparison of clinical results performed with different instruments. Within the framework of different European projects (MEDPHOT, OPTIMAMM, nEUROPt, LaserLabEurope), common protocols and related phantom kits have been developed to provide guidelines for the comparison of various diffuse optics systems. In particular, the performance assessment of TD fNIRS instruments was addressed in the nEUROPt project with the adoption of 3 protocols agreed upon by a cluster of 17 institutions.

These include the "Basic instrumental performance" protocol to characterize key hardware specifications of TD fNIRS systems (e.g. FWHM of the IRF, drift of laser power or timing) that are crucial for the outcome of the clinical measurements (Wabnitz et al., 2011).

The MEDPHOT protocol (Pifferi et al., 2005) was ~~finalized~~ adapted to TD fNIRS systems in order to characterize~~s~~ the capability ~~to~~ of an instrument to measure the optical properties (absorption coefficient and reduced scattering coefficient) of a homogeneous diffusive medium by assessing accuracy, linearity, noise, stability, and reproducibility of these measurements.

Finally, the nEUROPt protocol was designed to address the capability of optical brain imagers to detect, localize and quantify changes in the optical properties of the brain (cerebral cortex) and to eliminate the influence of extra-cerebral tissues on the measurement. A specific inhomogeneous phantom was designed to reliably mimic absorption changes in the cortex as the most relevant physical quantity in neurological applications of diffuse optical imaging (Wabnitz et al., 2013)

Common efforts are being currently pursued to further promote standardization issues in the scientific community both for TD and CW regimes. A joint initiative of the International Electrotechnical Commission (IEC) and of the International Organization for Standardization (ISO), leaded by Prof. Hideo Eda (The Graduate School for the creation of new Photonics industries, Hamamatsu, Shizuoka, Japan), with the support of Physikalisch-Technische Bundesanstalt, Berlin and Politecnico di Milano, Milan, for actions at the local (national) level in Germany and Italy, has been started, aiming at defining a simple, easy to use standard. The proposed project is carried out by technical committee ISO/TC 121/SC 3 and IEC/SC 62D JWG 5 under the IEC lead. (IEC, 2013).

Finally it is worth mentioning that TD fNIRS data type (as well as CW and FD data types) will be inserted in the Shared Near Infrared File Format Specification, a recent initiative for standardization of data types triggered by the fNIRS community (Frederick and Boas, 2013).

TD fNIRS features

In this section we present the main features (or fingerprints) of TD fNIRS, aiming at elucidating the differences and advantages with respect to CW fNIRS and its drawbacks. We focus on the issues of quantification, penetration depth, depth selectivity, spatial resolution, and contrast-to-noise ratio. As a general aspect we note that these issues are strongly entangled since the common underlying physical phenomena is the interplay between light absorption and light diffusion at the microscopic scale. However, for the sake of clarity we try to distinguish the main peculiarity of each presented issue. We conclude this section with representative *in vivo* data obtained with a TD fNIRS system.

Quantification

Probably the oldest argument in favor of the TD approach is that of discrimination and quantification of the optical properties, namely the absorption coefficient and reduced scattering coefficient, the former being related to tissue constituents, the latter to tissue structures (Jacques, 1989b). Absolute estimate of the absorption coefficient would allow the derivation of SO_2, a crucial parameter for many neurological conditions (Maas and Citerio, 2010).

~~Indeed~~ However this~~the~~ advantage of TD NIRS strictly holds in a homogeneous medium. A TD NIRS measurement at a single source detector distance allows a complete optical characterization of the probed tissue, without the complicated multi-distance arrangements and the cumbersome calibration procedure that are needed for CW NIRS and FD NIRS. A few CW NIRS commercial systems have implemented a multi-distance approach (also called space-resolved spectroscopy, SRS) and yield parameters related to SO_2, assuming a constant and spectrally flat scattering coefficient (Wolf et al., 2007).

~~If we are~~When dealing with more complex geometries, the use of TD NIRS is likely to become less immediate. In a two-layered medium accurate estimates of the optical parameters have been obtained, provided a multi-distance (Martelli et al., 2003; Martelli et al., 2004) or a multi-distance and multi-wavelength (Pifferi et al., 2001) TD approach is used. In the case of a real tissue, like the human head, a two-layered model could be a too ~~approximated~~ simple approximation, and the use of priors of the true geometry (e.g. from anatomical 3D MRI maps or atlas), would be a prerequisite for setting up the forward problem by numerical methods like FEM or Monte Carlo. Absolute quantification of the optical properties in a real head is still an open issue. A recent collaboration among research groups in the framework of the European project nEUROPt is addressing the problem with a step by step approach involving multiple techniques (e.g. CW NIRS at multiple short distances to provide information on the superficial layer, to be used as priors for multi-distance and multi-wavelength TD NIRS in a layered model) (Foschum et al., 2012).

The two-layer approach was implemented on TD NIRS data on the adult head (Gagnon et al., 2008), and reported a clear distinction between extra- and intra-cerebral optical properties, even though the values could not be validated by independent modalities.

In many applications of interest in the neuroimaging community fNIRS looks for changes with respect to a baseline. Only the few FD or SRS CW fNIRS systems, implementing the multi-distance approach, aim at providing absolute changes, while the majority of single source detector distance CW fNIRS devices just provide relative changes. TD fNIRS can be of help since, with limited assumptions on the baseline optical properties (a rough estimate can be always obtained by fitting with the homogeneous model), average photon path length (equivalently the average time spent by photon) can be estimated in different head compartments (at least the extra-cerebral and the intra-cerebral ones) allowing for absolute estimate of absorption changes. Expressions to estimate the absorption changes have been reported in *Appendix*. In the following *Depth selectivity* section we will provide further comments on the quantification of absorption changes based on an experimental validation.

Penetration depth

For fNIRS applications aiming at mapping the functioning of human brain, the ability to probe the measured tissue in depth is of the utmost importance. NIRS light has in fact to cross through the scalp, the skull and the cerebrospinal fluid before reaching the brain, and NIRS photons have to travel back to head surface to be eventually detected. In the adult head the mean thickness of the skull has been measured in the range from 5.3 mm to 7.5 mm (Moreira-Gonzalez et al., 2006), and the average distance between the cortical surface and the head surface along the scalp was estimated to be in the range of 10-30 mm depending on the location (Okamoto et al., 2004).

To properly probe the cortical region a source-detector distance of 30-40 mm is typically used in many CW fNIRS devices, while shorter distances (20-30 mm) proved to be more efficient in newborns taken into account the reduced head size (Dehaes et al., 2011b; Gervain al., 2011). This is in agreement with theoretical expectations. In CW NIRS, photons emerging at larger source detector distances have travelled longer paths deeper inside the medium, and thus they carry more information on deeper tissues (Feng et al., 1995; Del Bianco et al., 2002).

TD fNIRS measurements on adult have been typically reported with source-detector distance in the range 20-30 mm. Indeed, in TD NIRS measurements the information on deeper tissues can be obtained from photons emerging with longer time-of-flight (Steinbrink et al., 2001), independently of the source detector distance (Del Bianco et al., 2002), as also demonstrated by the null distance TD NIRS approach (Torricelli et al., 2005; Spinelli et al., 2006; Pifferi et al., 2008).

Fig. 4 and Fig.5 show the results of simulations performed to obtain the sensitivity profiles and maps for different source detector distances in a homogeneous medium and in a human head, respectively. It is evident that in both cases penetration depth increases with time and not with source detector distance. Fig. 6 presents the results of a simple experiment (from the nEUROPt protocol) that can be effectively used to test penetration depth. A black PVC cylinder (volume 500 mm^3) is embedded in a liquid diffusive medium with average optical properties mimicking a human head (μ_a = 0.01 mm^{-1}, μ_s' = 1.0 mm^{-1}). The cylinder is positioned in the mid plane between source and detector (at a distance of 30 mm) and its depth is varied in the range 6-40 mm. The system setup is described in Contini et al. (2013a). As shown in panel 6(a), the contrast for an early time-gate (500 ps) is high if the perturbation is located close to the surface, while it diminishes rapidly as the perturbation depth increases. Conversely a late time-gate (e.g. 2500 ps) has a lower contrast for perturbation with shallow depth, while the contrast increases as a function of perturbation depth, reaching a maximum and then going to zero. We observe that the contrast is small but not negligible even at a depth of 30 mm for the late gate at 3500 ps. The contrast for the CW case (obtained by summing photons detected at any time) is also shown. The dependence of the contrast ~~from~~ on the photon time-of-flight ~~of~~ is plotted in panel 6(b) for different depths of the perturbation. It is clear that the optimum time-gate moves to longer time as the perturbation goes deeper in the medium, although the contrast inevitably diminishes.

Further, we recall that in CW fNIRS background absorption strongly affects penetration depth by preferentially reducing the number of long lived (i.e. deeper) photons. Instead, in TD fNIRS the penetration depth is independent from the background absorption (Del Bianco et al., 2002). Actually, a photon behaves in the same way independently from the used detection technique. Consequently, as shown in Fig.1, in TD fNIRS an increase in absorption determines a reduction in the number of photons with longer time-of-flight (the longer the time-of-flight, the higher the probability of being absorbed). Hence absorption does have an effect on penetration depth in TD fNIRS since it reduces the temporal dynamics (at the microscopic level). Indeed this effect can be properly compensated by increasing the injected power (if available, and if within the safety limits). Nothing can be done in CW fNIRS to overcome the effect of background absorption. One could argue that it is unlikely that during an experiment the background absorption varies significantly. Unfortunately this could be the case for systemic (global) effects that affect blood perfusion. From a more technical point of view, there is an advantage related to the independence of TD fNIRS from background absorption. For a multi-wavelength approach, where the use of spectral priors is aimed at improving the accuracy of the estimate of hemodynamic parameters, the TD penetration depth will be to a first approximation spectrally flat since it would depend only on the smooth spectral dependence of the scattering.

These considerations hold true not only in a homogeneous medium, where the relationship among absorption, photon time-of-flight and penetration depth can be obvious, but also in more complex situations ~~like~~ such as a layered medium with different optical properties (e.g. the human head).

Depth selectivity

To improve depth selectivity, that is ~~the rejection~~to reject ~~of~~ superficial extra-cerebral contributions, is a major challenge in fNIRS in both adults and newborns (Takahashi et al., 2011; Kirilina et al., 2012; Gagnon et al., 2012b; Aslin, 2013). In CW fNIRS this can be ~~obtained~~ achieved by adding a short distance (< 5 mm) channel with enhanced sensitivity to superficial layer (Saager et al., 2011, Gagnon et al., 2012a; Scarpa et al., 2013), or by means of a more sophisticated tomographic approach exploiting a dense arrangement of the optodes (Eggebrecht et al., 2012). Nonetheless, we stress that no depth selectivity is achievable with a single source detector distance CW fNIRS device. Postural, mechanical, and neural changes, which may occur under most investigative maneuvers, alter blood perfusion or/and distribution in the extra-cranial compartment and affect CW fNIRS variables to the extent that detected changes in cerebral tissue blood volume and oxygenation can be frequently reversed (Canova et al., 2011).

On the other hand, in single source detector distance (either large or small) TD fNIRS depth selectivity is improved by contrasting the signal obtained after integration of photons detected at early and late time-windows (Selb et al., 2005; Contini et al., 2007), or, similarly, by contrasting the moments of the DTOF (Liebert et al., 2004, Liebert et al., 2012; Hervè et al., 2012).

A significant modification of the instrumentation is required in CW fNIRS to implement the multi-distance approach. Conversely, since TD fNIRS naturally measures photon time-of-flight, it just requires post processing analysis to discriminate intra-cranial and extra-cranial contributions. The TD approach based on time-windows or moments is also efficient for identifying other artifacts related to superficial phenomena, e.g. the detachment of an optode (Gibson et al., 2006).

A simple experiment (from the nEUROPt protocol) can be devised to test depth selectivity. In a two-layer diffusive phantom (see Del Bianco et al. 2004 for details on the construction of the phantom) absorption changes either in the upper or in the lower layer have been produced by adding known amounts of a calibrated black ink. The corresponding contrasts for different time-gates (constant width: 500 ps, increasing delay: 500, 1000, 2000, and 4000 ps) and for the CW case (delay: 0 ps, width: 0-5000 ps,) have been calculated according to formula A1 reported in *Appendix* and are shown in Fig.7. When the absorption changes in the upper layer, all time-gates are affected (all photons travel in the superficial layer since they are injected from the external upper surface). In particular we observe that the contrast is even higher for late gates, since long lived photons have a higher probability of being absorbed,

independently of the location of the absorption perturbation. When the absorption changes are produced in the lower layer, the early gates have negligible or small contrast, as expected, since they have a reduced probability to reach the lower layer and then be reemitted at the surface. The contrast for the CW case is also reported and it is in general closer to the early than to the late gates (the majority of photons are in fact collected at early gates and they contribute largely to the CW signal). The changes in the absorption coefficient are then estimated with the formulas A3-A7 reported in *Appendix*. The use of an early time-window can provide a sufficiently accurate estimate of the absorption changes when they affect the upper layer (see panel 7(b)). In the same situation, a very late time-window is able to yield an estimate of the absorption changes in the lower layer that is minimally affected by the changes in the upper layer (especially if correction methods, described by Eq. A6 and A7 are used). The problem of accuracy related to the estimate of photon path-length in the different layers of the medium is still an open issue in the case of changes affecting the lower layer. As shown in panel 7(d), linearity with the perturbation is achieved, but quantification is definitely poor. Nonetheless, the estimates obtained with the TD approach are catching the phenomenological effects occurring either in the upper or in the lower layer. More accurate estimates could be obtained with methods based on the moments of the DTOF (Liebert et al., 2012).

Spatial resolution

Light diffusion is the enabling mechanism in fNIRS since it allows photons to penetrate deeply in biological tissues and to be diffusely reemitted, carrying the information on deep structures. However, light diffusion itself strongly limits the achievable spatial resolution in fNIRS to a value of the order of 10 mm (Boas et al., 1994).

When dealing with spatial resolution in fNIRS it is useful to distinguish between lateral and depth resolution. Lateral resolution ~~is measured looking at two perpendicular directions parallel to the (head) surface. This parameter~~ depends on source detector distance, therefore it ~~could~~ can be improved by the use of multi-distance or tomographic detection schemes in both TD and CW fNIRS (Gao et al., 2004; ~~Boas~~ Arridge et al., 2011) or of the null distance approach in TD fNIRS (Torricelli et al., 2005). ~~Lateral resolution~~This parameter is also influenced by penetration depth and depth selectivity, therefore comparisons of lateral resolutions should be~~tests are~~ made at a fixed depth, typically 10 mm to mimic the average equivalent distance of brain cortex to the scalp (Wabnitz et al., 2013).

Depth resolution explores the direction orthogonal to and beneath the (head) surface. In TD fNIRS depth resolution depends on photon time-of-flight and scattering properties (Steinbrink et al., 2001; Liebert et al.,2004; Spinelli et al., 2009b), while for CW fNIRS it depends on source detector distance, scattering and absorption (Del Bianco et al., 2002). Similarly to lateral resolution, depth resolution can be

influenced by the ability of the system to reject confounding superficial phenomena (i.e. extra-cerebral, systemic responses).

Broadening of the IRF has detrimental effects on depth resolution ~~(and also~~as well as on penetration depth, depth selectivity, and contrast~~)~~, and its influence ~~would be~~is larger ~~if the~~for smaller source detector distance ~~is narrower~~ (Pifferi et al., 2010). A simple intuitive reason for this later aspect is the fact that the larger the source detector distance, the broader in time ~~is~~ the measured DTOF is ~~as~~ compared to the IRF. If a better system with a narrower IRF ~~could not~~cannot be designed, ~~there could be~~ the possibility remains to partially overcome these limitations by employing convolution or deconvolution procedures. Convolution of the IRF with a theoretical model before fitting experimental DTOF proved to be effective for an accurate estimate of optical properties (Cubeddu et al., 1996; Spinelli et al., 2009a). In the past, deconvolution algorithms had the reputation of introducing noise in the computation and were rarely used. Recently improved deconvolution algorithms have been developed and tested (Hebden et al., 2003; Bodi and Bérubé-Lauzière, 2009, Diop and St Lawrence, 2012). To tackle the IRF problem, an elegant method is ~~that~~ the use of moments of the DTOF since ~~there is the advantage that~~ no deconvolution of the DTOF by the measured IRF is needed. The moments calculated from the measured DTOFs can, in fact, be corrected for the IRF simply by subtracting the corresponding moments of the IRF to obtain the true moments (Liebert et al., 2004; Hervé et al., 2012). ~~Indeed,~~However, since the moments are global parameters calculated by integrating the DTOF (therefore mixing early and late arriving photons), this semi-empirical approach can not totally circumvent the uncertainty in photon timing due to a broad IRF, therefore depth resolution is not likely to improve.

Finally, we observe that for TD fNIRS the fundamental physical limit to depth resolution is imposed by scattering. In the ideal case of a delta-like IRF (in practice a temporal resolution of < 1 ps that could be obtained, for instance by using ultrafast laser with fs pulse duration and a streak camera system, coupled to zero dispersion optical fibers), it would be impossible to discriminate deep absorbing structures with a resolution better than 5 mm. The possibility to finely discriminate deep structures in diffusive media is therefore limited to the very superficial layers (i.e. depth << 5 mm), but in this case other advanced optical techniques like optical coherence tomography (Fujimoto et al., 1995; Aguirre et al. 2006) and laminar optical tomography (Dunn and Boas, 2000; Hillman et al., 2004) are able to provide sharp results. These methods can be used for *in vivo* optical imaging of the exposed cortex. A review on the effect of light scattering on depth resolution is provided by Hillman et al. (2011).

Contrast-to-noise ratio

The overall ability of an fNIRS system of detecting a cortical response depends on many factors (e.g. depth, simultaneous presence of superficial systemic response, IRF), as discussed in the previous sections.

A single parameter to synthetically gauge an fNIRS system can be the contrast-to-noise ratio (CNR). The CNR takes into account the sensitivity of the system to changes in the measured quantity (e.g. light attenuation in CW fNIRS, intensity integrated in a given time-window in TD fNIRS) and it relates this change (contrast) to the noise level, as determined – for instance – by the standard deviation of the measured quantity, typically estimated during a resting period (baseline).

The contrast for a TD fNIRS measurement can be higher than for the CW case, simply because it is possible to extract long-lived photons that have traveled a larger fraction of their path in the deeper cortical region as compared to the mean photon distribution collected in a CW measurement. Also, tighter spatial confinement attainable upon reducing the source detector distance – for a fixed photon travelling time – leads to an increase in contrast.

Conversely, the real bottleneck of actual TD systems is the noise level. If the TCSPC technique is used – possibly the most popular choice – the maximum count rate per channel is limited to a few 10^6 photons/s due to the single-photon counting statistics and minimum dead time of the electronics. This limits the maximum signal level that can be extracted in a TD measurement and thus constrains the CNR. Further, amplitude stability and overall detection responsivity are typically worse in a TD system simply because the need to achieve temporal information reduces the choice of sources and detectors. Finally, the total number of parallel running sources and detectors is typically lower due to the intrinsic higher complexity and cost of single devices.

Fig.8 shows the CNR as function of depth for different time gates. We observe that the CNR value reported for the CW case is not the best estimate, since CW data have been obtained with a TD system by integrating all the detected photons. We expect that a real CW system performs in a much better way. An experimental comparison of the TD and CW approaches would be appropriate, but it is not within the scope of this review.

Representative in vivo *data*

To better illustrate the specific information that can be obtained by TD fNIRS we report on two simple case studies: a motor task experiment and a Valsalva maneuver.

For both studies the TD fNIRS medical device (working at 690 nm and 830 nm) described in Contini et al. (2006) was used, a single channel (source detector distance 20 mm) was centered over the C3 point, and data were acquired at 1Hz.

In the motor task experiment the protocol consisted in 20 s baseline, 20 s finger tapping with the right hand at 2 Hz, and 40 s recovery. Ten repetitions were performed and averaged. In the Valsalva maneuver experiment the protocol consisted in 20 s baseline, 20 s expiring through a closed mouthpiece, and 40 s recovery. Five repetitions were performed and averaged.

In both experiments, for each wavelength and all repetitions, we calculated the contrast C, the absorption changes in the intra-cerebral and extra-cerebral region, and the O_2Hb and HHb time courses as described in *Appendix*.

Fig. 9(a-g) reports the contrast C during the finger tapping experiment for different time-gates with constant width (250 ps) and increasing delay (from 0 to 12000 in 250 ps steps, then 1500 ps and 2000 ps). ~~, and for the CW case (as a time window with 0 ps delay and 2500 ps width).~~ For both 690 nm and 830 nm the contrast is rather flat and close to zero during the baseline, as expected. Then during the task it increases at 830 nm, while it decreases at 690 nm. These changes are greater for later time-gates. The maximum value of the contrast during the task period at 830 nm in fact almost doubles its value, from 0.04 at the earliest gate (delay 0 ps) to 0.07 for the latest time-gate (delay 2000 ps). Similarly, at 690 nm the contrast is three times higher at the latest time-gate (C=-0.06) with respect to the earliest time-gate (C=-0.02). This is an indication that a deep perturbation is present. Indeed by looking at the contrast at the very early time-gates, it is possible to observe that the contrast at 830 nm presents large periodic changes, only partially related to the task, with a triangular or saw-tooth shape, not resembling a typical task-evoked cerebral hemodynamic response. We note that the same time course is present at least qualitatively also at longer time-gates, and this is expected since superficial changes affect photons detected at any time, as described in previous sections. Conversely, the time course for 690 nm does not present this features. As recently reported by Kirilina et al. (2012), this could likely be the effect of task-evoked systemic changes.

Fig. 9(h-j) reports the time course of the moments of the DTOF. The contrast from the lowest order moment (related to the CW intensity) is greatly affected by systemic changes, while higher order moments are less affected.

Fig. 9(k-o~~b~~) reports the time course for the estimates of O_2Hb and HHb for the extra-cerebral region, for the intra-cerebral region (without and with correction for changes in the extra-cerebral region), and the global estimate from the CW case. In the extra-cerebral region the O_2Hb signal presents the task-evoked changes, while the HHb presents a limited decrease. In the intra-cerebral region the task-evoked perturbation in O_2Hb still appears, while it is almost canceled if we use the correction for the superficial disturbances. In the CW, the systemic task-evoked effect is clearly visible.

Fig. 10(a-g) reports the contrast C during the Valsalva maneuver for different time-gates with constant width (250 ps) and increasing delay (from 0 to 1000 in 250 ps steps, then 1500 ps and 2000 ps~~from 0 to 2000 in 250 ps steps), and for the CW case (as a time window with 0 ps delay and 2500 ps width)~~). For both 690 nm and 830 nm the contrast during the task greatly increases with respect to the baseline period. This holds true at any time-gate, with a limited increase when moving from early to late gate: the contrast at 690 nm changes from 0.15 to 0.25, at 830 nm from 0.10 to 0.15). This suggests the presence of a

superficial absorption perturbation with a limited effect on deeper regions, as expected (Canova et al., 2011). This is confirmed by the time courses of the moments of the DTOF (see Fig. 10(h-j)) and by the time courses of O_2Hb and HHb for the extra-cerebral region and for the intra-cerebral region, if for the latter case the correction for changes in superficial layers is applied. We note that both the uncorrected intra-cerebral response and the CW response are largely affected by the superficial effects (see Fig. 10(k-o~~b~~)).

Future perspectives

In this section we briefly present the foreseen advances at both the technological and modeling level from which TD fNIRS could benefit in the next years.

There are several technological improvements in light sources, detection techniques and delivery and collection systems that could significantly enhance TD fNIRS overall performances in the next years. The SC fiber laser (Fianium, 2013b; NKT Photonics, 2013b) has been recently introduced in TD fNIRS systems and their potential has not been fully proved. They are compact and could nicely fit in trolley and rack for medical device. They provide narrow pulses at any level of power, without degrading the IRF. Indeed, they are to some extent a very inefficient solution since the available power is spread over a wavelength range much larger than the useful range. On one hand, excess power in unused wavelength intervals (e.g. < 600 nm, > 900 nm) have to be properly attenuated (e.g. by using dichroic mirror of hot filter) so as not to direct it to the sample under test. On the other hand, power spectral density is limited and sufficient power levels for application in the real environment are obtained summing up the power at adjacent wavelengths (up to 40 nm in some cases), at the cost of reducing the spectral purity of the injected pulses, and the overall accuracy in the reconstruction if the bandwidth is not taken into account (Farina et al., 2009). Consequently, a SC with reduced width, covering the proper spectral range while maintaining a high conversion rate, is desirable.

As an alternative to SC lasers, picosecond pulsed laser diode heads based on a master oscillator fiber amplifier concept can offer pulse widths <100 ps and average powers up to 1 W (depending on wavelength). The drawback at the moment of writing is the limited availability of wavelengths (e.g. 531 nm, 710 nm, 766 nm, 1064 nm and 1530 nm) (PicoQuant GmbH, 2013c; Fianium, 2013a).

The ~~S~~silicon p~~P~~hotonics field is promising compact and scalable devices and components for telecommunications, but unfortunately they are not produced in the wavelength range of interest for fNIRS (Fang and Zhao, 2012). Similarly several optical components and devices for properly handling light pulses at the picosecond level have been devised in the fields of ~~Photonics~~ photonics and ~~Communications~~ communications by exploiting the recent studies on metamaterials (Liu and Zhang,

2011), and chalcogenide materials (Eggleton et al., 2011). Again, there are no fundamental limitations that prevent the designing of specific components for operation in the spectral range of interest for fNIRS. Also delivery and collection systems could be positively influenced by the advances in Photonics . To mention a specific case, we observe that nowadays commercial products exist that are able to overcome some of the basic limitations of classical optical fiber. Photonic crystal fibers (PCF) have in fact been recently produced operating as single mode over a broad spectral range (NKT Photonics, 2013a). A conventional single mode optical fiber is actually multimode for wavelengths shorter than the second-mode cutoff wavelength, limiting the useful operating wavelength range in many applications. With PCF we could think to overcome most of the ~~annoying~~ limitations of multimode SI fiber bundles that are used for light collection in TD fNIRS.

For what concerns the detection techniques, we observe that the main drawbacks of existing TCSPC systems are actually not set by physical limits, and they could be overcome by technological advancements. As a side product of the research on the null distance TD approach, ultra-fast time gating circuits and electronics have been developed, that could improve the performances of modern detection techniques like TCSPC (the limits in photon counting statistics holds but with the time gating approach we are for example able to count only useful photons in specific time-windows). In particular time-to-digital conversion (TDC) electronics, could replace modern TCSPC modules for aiming at a higher integration level (Mata Pavia et al., 2012). Similarly advanced photodetectors, like SPAD with enhanced sensitivity, large area SPAD, SPAD array or matrix with improved performances could be designed and fabricated (Micro Photon Devices, 2013b; Micro Photon Devices, 2013c).

Similarly, the modeling used for the interpretation of real data is nowadays too elementary. Advanced computational tools for modeling light propagation in the head are available, but to date they have been used mostly for simulations, while rarely for the *in vivo* data analysis. The situation is different for the CW case where sophisticated approaches to data analysis have been successfully proposed (Tsuzuki et al., 2007; Custo et al., 2010; Tsuzuki et al., 2012; Cooper et al., 2012a). In most clinical studies the head is approximated as homogeneous or two layered medium. This approach might have the advantage of robustness but it definitely fails in terms of accuracy. The use of priors (e.g. anatomical, optical, or spectral) would greatly improve the accuracy of the results, but in most cases at the cost of a very high computational load. Parallel computing algorithms and platforms are therefore required to make this affordable.

Conclusions

We have presented a comprehensive and critical review on TD fNIRS in which we have highlighted that TD fNIRS could play a significant role not only as a complex research tool at the laboratory stage, but also as a powerful instrument for all fNIRS applications.

As a general comment we note that an ideal TD fNIRS system might not exist. However, the design of novel instruments can be properly tailored to the specific needs of the end-users at both research and clinical level. The performances, the complexity, as well as the costs of a TD fNIRS system can significantly vary depending for example on the number of independent channels.

Interestingly, TD NIRS systems and devices have found applications in other fields ~~like~~ such as optical mammography, and molecular imaging of small animals. The eventual growth and broader diffusion of these applications would further foster TD fNIRS. By synergic and collaborative efforts among experts in Photonics, Electronics, Information technology and Neuroscience we foresee a flourishing future for TD fNIRS.

We persuasively conclude this review by quoting the 17th century English philosopher and scientist Francis Bacon: "Truth is rightly named the daughter of ***time***" (Novum Organum, 1620).

Acknowledgements

The Authors are thankful to many colleagues and friends for helpful and illuminating discussions during the past years. We would like to kindly mention: Prof. Rinaldo Cubeddu, Alberto Dalla Mora, Laura di Sieno (Politecnico di Milano, Dipartimento di Fisica); Fabrizio Martelli and Giovanni Zaccanti (University of Florence, Italy); Alberto Tosi and Franco Zappa (Politecnico di Milano, Dipartimento di Elettronica ed Informazione). In addition all researchers in the narrow TD fNIRS community, with special remarks for Heidrun Wabnitz and Rainer Macdonald (Physikalisch-Technische Bundesanstalt, Berlin, Germany), Adam Liebert and Roman Maniewski (Institute of Biocybernetics and Biomedical Engineering, Warsaw, Poland), Alwin Kienle (Institut für Lasertechnologien in der Medizin und Meßtechnik an der Universitaet Ulm, Germany), Hellmuth Obrig (Max-Planck-Institut für Kognitions- und Neurowissenschaften, Leipzig, Germany), Jens Steinbrink (Charité Universitaetsmedizin ,Berlin, Germany), Jeremy Hebden and Simon Arridge (University College London, United Kingdom), Juliette Selb and David Boas (Massachusetts General Hospital, Athinoula A. Martinos Center, Charlestown, Massachusetts). A particular thanks also to Martin Wolf (University Hospital Zurich, Switzerland), Jacques Mehler (Scuola Internazionale Superiore di Studi Avanzati, Trieste, Italy), Luciano Fadiga (University of Ferrara, Italy), Patrizia Baraldi (University of Modena, Italy) and Simone Cutini (Università di Padova). Finally, Marco Ferrari and Valentina Quaresima (Università di L'Aquila, Italy) have supported with their passion and expertise our steps in the fNIRS field.

The research leading to these results has partially received funding from the European Community's Seventh Framework Programme under the nEUROPt Project (grant agreement FP7-HEALTH-2007-201076).

Appendix

The concentration changes of O_2Hb and HHb were obtained from the changes in light attenuation ~~changes as obtained by~~after integrating photons in different time-windows.

For each wavelength, we calculated the contrast, defined as

$$C(d,w;T;\lambda) = -\ln[N(d,w;T;\lambda)/N_0(d,w;\lambda)] \quad \text{A1}$$

where $N(d,w;T;\lambda)$ is the number of photons collected in a time window with delay d and width w, at macroscopic (experiment) time T for wavelength λ, and $N_0(d,w;\lambda)$ is the number of photons collected in the very same time window and for the same wavelength, averaged over the baseline period of the protocol.

Changes in the absorption coefficient for each wavelength λ and at any time T are estimated with the formula

$$\Delta\mu_a(T;\lambda) = C(d,w;T;\lambda)/L \quad \text{A2}$$

where L is the photon path-length (Nomura et al., 1997).

A rough assumption for the path-length is $L = vt$, where v is the speed of light in the medium and t is the average photon-time-of-flight. Taking into account the dependence of penetration depth ~~to~~ on photon time-of-flight, by properly selecting an early time-gate it is possible to estimate changes in more superficial layers (i.e. extra-cerebral), while a late time-gate yields information on deeper regions (i.e. intra-cerebral). The formulas for the absorption changes can then be specified as follow:

$$\Delta\mu_a^{EXTRA}(T;\lambda) = C(d_E,w_E;T;\lambda)/L_E \quad \text{A3}$$

$$\Delta\mu_a^{INTRA}(T;\lambda) = C(d_L,w_L;T;\lambda)/L_L \quad \text{A4}$$

where d_E, w_E, and L_E (d_L, w_L, and L_L) are proper delay, width and path-length of the time-gate to select early (late) arriving photons.

By integrating all detected photons (e.g. selecting a time-window with delay $d_{CW} = 0$ ps and width $w_{CW} = 5000$ ps) it is possible to address the CW case. As photon path-length we use $L_{CW} = v\langle t\rangle$, where $\langle t\rangle$ is the mean time-of-flight (first order moment of the DTOF). The corresponding absorption change is then calculated as

$$\Delta\mu_a^{CW}(T;\lambda) = C(d_{CW},w_{CW};T;\lambda)/L_{CW} \quad \text{A5}$$

This is equivalent to the modified Beer–Lambert law with differential path-length factors (DPF) not taken from the literature but estimated directly by the DTOF.

To enhance the contribution from deep layers and to remove possible disturbances caused by superficial ones, correction methods (Selb et al., 2005; Contini et al., 2007) are also used for the intra-cerebral changes:

$$\Delta\mu_a^{INTRA}(T;\lambda) = [C(d_L,w;T;\lambda) - C(d_E,w;T;\lambda)]/L_L \quad \text{A6}$$

Formatted: Font: Symbol, Not Bold, French (France)

$$\Delta\mu_a^{INTRA}(T;\lambda) = \{ln[N(d_L,w_L;T;\lambda)/N_0(d_L,w_L;\lambda)] - ln[N(d_E,w_E;T;\lambda)/N_0(d_E,w_E;\lambda)]+1\}/L_L \quad A7$$

Finally, ~~taking~~ making the assumption that hemoglobin is the only chromophore contributing to absorption, O_2Hb and HHb concentration changes are then derived by Lambert Beer law, using the hemoglobin absorption spectra from Prahl et al. (2013).

Changes of moments of DTOFs are defined as in Liebert et al. (2004):

$$\Delta A(T;\lambda) = -ln[N(T;\lambda)/N_0(\lambda)] \quad A8$$

$$\Delta\langle t(T;\lambda)\rangle = \langle t(T;\lambda)\rangle - \langle t_0(T;\lambda)\rangle \quad A9$$

$$\Delta V(T;\lambda) = V(T;\lambda) - V_0(T;\lambda) \quad A10$$

where ΔA is the change in attenuation, N is the total number of photons (0^{th} order moment of DTOF, corresponding to the number of photons collected in a time window with delay 0 and width ∞), $\langle t\rangle$ the mean photon time-of-flight (1^{st} order moment) and V is the variance (second centralized moment of the DTOF). The quantities with index 0 refer to the signal recorded during a reference period (e.g. the rest period before stimulation).

Formatted: Font: Symbol, Not Bold, French (France)

Formatted: Space After: 0 pt

Field Code Changed

References

Advanced Laser Diode Systems GmbH, 2013. PiLas. http://www.alsgmbh.com/pilas.htm.

Advanced Research Technologies (ART), 2013. Optix MX3 - Pre-Clinical Optical Molecular Imager. http://www.art.ca.

Aguirre, A.D., Chen, Y., Fujimoto, J.G., Ruvinskaya, L., Devor, A., Boas, D.A., 2006. Depth-resolved imaging of functional activation in the rat cerebral cortex using optical coherence tomography. Opt. Lett. 31(23), 3459–3461.

Alerstam, E., Andersson-Engels, S., Svensson, T., 2008a. Improved accuracy in time-resolved diffuse reflectance spectroscopy. Optics Express 16(14), 10440-10454.

Alerstam, E., Svensson, T., Andersson-Engels, S., 2008b. Parallel computing with graphics processing units for high-speed Monte Carlo simulation of photon migration. J. Biomed. Opt. 13(6), 060504.

Aletti, F., Re, R., Pace, V., Contini, D., Molteni, E., Cerutti, S., Maria Bianchi, A., Torricelli, A., Spinelli, L., Cubeddu, R., Baselli, G., 2012. Deep and surface hemodynamic signal from functional time resolved transcranial near infrared spectroscopy compared to skin flowmotion. Computers in Biology and Medicine 42(3), 282-289.

Alphalas GmbH, 2013. PICOPOWER™-LD Series. http://www.alphalas.com/products/lasers/picosecond-pulse-diode-lasers-with-driver-picopower-ld-series.html.

Arridge, S.R., 1999. Optical tomography in medical imaging. Inverse Problems 15, R41-R93.

Arridge, S.R., Schweiger, M., Hiraoka, M., D.T. Delpy, D.T., 1993. A finite element approach for modeling photon transport in tissue. Med. Phys. 20(2), 299-309.

Arridge, S.R., Schweiger, M., Schotland, J.C., 2011. Inverse Model in Light Transport. In Handbook of Biomedical Optics, Part III, Chap. 17. Boas, D.A., Pitris, C., Ramanujam, N., (Eds.) CRC Press Boca Raton, Florida.

Aslin, R.N., 2013. Questioning the questions that have been asked about the infant brain using NIRS. Cognitive Neuropsychology, 29, 7-33.

Austin, T., Gibson, A.P., Branco, G., Yusof, R.Md., Arridge, S.R., Meek, J.H., Wyatt, J.S., Delpy, D.T., Hebden, J.C., 2006. Three-dimensional optical imaging of blood volume and oxygenation in the preterm brain. NeuroImage. 31(4), 1426-1433.

Formatted: Font: Not Bold, Italian (Italy)

Formatted: Italian (Italy)

Formatted: Font: Not Bold, Italian (Italy)

Formatted: German (Germany)

Formatted: Font: Not Bold, German (Germany)

Formatted: Font: Not Bold, Italian (Italy)

Formatted: Italian (Italy)

Bari, V., Calcagnile, P., Molteni, E., Re, R., Contini, D., Spinelli, L., Caffini, M., Torricelli, A., Cubeddu, R., Cerutti, S., Bianchi, A.M., 2012. From neurovascular coupling to neurovascular cascade: a study on neural, autonomic and vascular transients in attention. Physiol. Meas. 33, 1379-1397.

Bassi, A., Brida, D., D'Andrea, C., Valentini, G., Cubeddu, R., De Silvestri, S., Cerullo, G., 2010. Time-gated optical projection tomography. Opt. Lett. 35, 2732-2734.

Becker & Hickl GmbH, 2013a. BHLP-700. http://www.becker-hickl.de/lasers.htm#BHLP-700.

Becker & Hickl GmbH, 2013b. Detectors for Photon Counting. http://www.becker-hickl.de/detectors.htm#HPM100-50

Becker & Hickl GmbH, 2013c. Simple-Tau 130 Table-Top TCSPC Systems. http://www.becker-hickl.com/simpleTau.htm#st140.

Becker & Hickl GmbH, 2013d. Time-Correlated Single Photon Counting Devices. http://www.becker-hickl.de/tcspc.htm.

Becker, W., 2005. Advanced time-correlated single-photon counting, Springer, Berlin, Heidelberg, New York.

Benaron, D.A., Hintz, S.R., Villringer, A., Boas, D., Kleinschmidt, A., Frahm, J., Hirth, C., Obrig, H., van Houten, J.C., Kermit, E.L., 2000. Noninvasive functional imaging of human brain using light. J. Cereb. Blood Flow Metab. 20, 469–477.

Boas, D.A, O'Leary, M.A., Chance, B.,Yodh, A.G., 1994. Scattering of diffuse photon density waves by spherical inhomogeneities within turbid media: Analytic solution and applications. Proc. Nati. Acad. Sci. USA, 91, 4887-4891.

Boas, D.A., Culver, J., Stott, J., Dunn, A., 2002. Three dimensional monte carlo code for photon migration through complex heterogeneous media including the adult human head. Opt Express 10, 159–70.

Boas, D.A., Dale, A.M., 2005. Simulation study of magnetic resonance imaging-guided cortically constrained diffuse optical tomography of human brain function. Applied Optics 44(10),1957–1968.

~~Boas, D.A., Pitris, C., Ramanujam, N., (Eds.), 2011, Chapter III Tomographic Imaging, in Handbook of Biomedical Optics, CRC Press Boca Raton, Florida.~~

Bodi, G., Bérubé-Lauzière, Y., 2009. A new deconvolution technique for time-domain signals in diffuse optical tomography without a priori information. Proc. SPIE 7369, 736914.

Formatted: Font: Not Bold, Italian (Italy)

Formatted: Font: Not Bold, Italian (Italy)

Formatted: Italian (Italy)

Formatted: Font: Not Bold, Italian (Italy)

Formatted: Font: Not Bold, German (Germany)

Formatted: German (Germany)

Formatted: Font: Not Bold, German (Germany)

Formatted: Font: Not Bold, Italian (Italy)

Formatted: Italian (Italy)

Formatted: Font: Not Bold, Italian (Italy)

Formatted: Font: Not Bold, Italian (Italy)

Formatted: Font: Not Bold, German (Germany)

Formatted: German (Germany)

Brühl, R., Kummrow, A., Möller, M., Wabnitz, H., Liebert, A., Ittermann, B., Seifert, F., Rinneberg, H., 2005. Concurrent Time-Resolved Near-Infrared Spectroscopy and fMRI Measurements of Visually Stimulated Humans., Proceedings of the 13th Scientific Meeting and Exhibition of the International Society for Magnetic Resonance in Medicine (ISMRM), 499.

Busch, D.R., Choe, R., Durduran, T., Baker, W.B., Foster, E.K., Averna, T.A., Friedman, D., Rosen, M.A., Schnall, M.D., Yodh, A.G., 2012. Microvascular Blood Flow Changes in Human Breast During Simulated Mammography. Biomedical Optics and 3D Imaging OSA 2012. Paper JM3A.13.

Butti, M., Contini, D., Molteni, E., Caffini, M., Spinelli, L., Baselli, G., Bianchi, A.M., Cerutti, S., Cubeddu, R., Torricelli, A., 2009. Effect of prolonged stimulation on cerebral hemodynamic: a time-resolved fNIRS study. Med. Phys. 36, 4103–4114.

Canova, D., Roatta, S., Bosone, D., Micieli, G., 2011. Inconsistent detection of changes in cerebral blood volume by near infrared spectroscopy in standard clinical tests. J. Appl. Physiol. 110, 1646-1655.

Chance, B., Leigh, J.S., Miyake, H., Smith, D.S., Nioka, S., Greenfeld, R., Finander, M., Kaufmann, K., Levy, W., Young, M., Cohen, P., Yoshioka, H., Boretsky, R., 1988. Comparison of time-unresolved measurements of deoxyhemoglobin in brain. Proc. Natl. Acad. Sci. U. S. A. 85, 4971–4975.

Chen, G.N., Zhu, Q., 2002. Time-resolved optical measurements with spread spectrum excitation. Opt. Lett. 27(20), 1806-1808.

Chen, G.N., Zhu, Q., 2003. Time-resolved diffusive optical imaging using pseudo-random bit sequences. Opt. Express 11(25) 3445-3454.

Coherent Inc., 2013. Ultrafast Ti:Sapphire Oscillators. http://www.coherent.com/Products/index.cfm?365/Ultrafast-Ti-Sapphire-Oscillators.

Collins, D.L., Zijdenbos, A.P., Kollokian, V., Sled, J., Kabani, N., Holmes, C., Evans, A., 1998. Design and construction of a realistic digital brain phantom. IEEE transactions on medical imaging. 17(3), 463-468.

Contini, D., Dalla Mora, A., Di Sieno, L., Tosi, A., Boso, G., Torricelli, A., Spinelli, L., Cubeddu, R., Pifferi, A., 2013a. Time resolved functional near infrared spectroscopy by means of time gated system at small interfiber distance. Oral communication at SPIE BiOS 2013 Conference 8578 Optical Tomography and Spectroscopy of Tissue X, 3 February 2013, Paper 8578-82.

Contini, D., Re, R., Turola, M., Spinelli, L., Romano, G., Cubeddu, R., Torricelli, A., 2013b. Multi-channel time-resolved functional near infrared spectroscopy system. Oral communication at SPIE BiOS

Formatted: Font: Not Bold, German (Germany)

Formatted: Font: Not Bold, Italian (Italy)

Formatted: Italian (Italy)

Formatted: Font: Not Bold, Italian (Italy)

Formatted: Font: Not Bold, Italian (Italy)

Formatted: Font: Not Bold, Italian (Italy)

Formatted: Italian (Italy)

Formatted: Font: Not Bold, Italian (Italy)

Formatted: Font: Not Bold, Italian (Italy)

Formatted: Italian (Italy)

Formatted: Font: Not Bold, Italian (Italy)

Formatted: Font: Not Bold, Italian (Italy)

2013 Conference 8578 Optical Tomography and Spectroscopy of Tissue X, 3 February 2013, Paper 8578-114.

Contini, D., Spinelli, L., Caffini, M., Cubeddu, R., Torricelli, A., 2009. A multichannel time-domain brain oximeter for clinical studies. Proc SPIE SPIE 7369, 73691D.

Contini, D., Torricelli, A., Pifferi, A., Spinelli, L., Cubeddu, R., 2007. Novel method for depth-resolved brain functional imaging by time-domain NIRS. Proc SPIE 6629, 662908.

Contini, D., Torricelli, A., Pifferi, A., Spinelli, L., Paglia, F., Cubeddu, R., 2006. Multichannel time-resolved system for functional near infrared spectroscopy. Opt. Express 14, 5418–5432.

Contini, D., Zucchelli, L., Spinelli, L., Caffini, M., Re, R., Pifferi, A., Cubeddu, R., Torricelli, A., 2012. Review: Brain and muscle near infrared spectroscopy/imaging techniques. Journal of Near Infrared Spectroscopy 20(1), 15-27.

Cooper, R.J., Caffini, M., Dubb,J., Fang, Q., Custo, A., Tsuzuki, D., Fischl, B., Wells III, W., Dan, I., Boas. D.A., 2012a. Validating atlas-guided DOT: A comparison of diffuse optical tomography informed by atlas and subject-specific anatomies. NeuroImage, 62(3), 1999-2006.

Cooper, R.J., Gagnon, L., Goldenholz, D., Boas, D.A. and Greve, D.N., 2012b. The utility of near-infrared spectroscopy in the regression of low-frequency physiological noise from functional magnetic resonance imaging data. NeuroImage 59(4), 3128–3138.

Cubeddu, R., Pifferi, A., Taroni, P., Torricelli, A., Valentini, G., 1996. Experimental Test of Theoretical Models for Time-Resolved Reflectance. Med. Phys. 23(9), 1625-1633.

Cubeddu, R., Pifferi, A., Taroni, P., Torricelli, A., Valentini, G., 1999. A compact tissue oximeter based on dual-wavelength multichannel time-resolved reflectance. Appl. Opt. 38, 3670–3680.

Custo, A., Boas, D.A., Tsuzuki, D., Dan, I., Mesquita, R., Fischl, B., Grimson, W.E.L., Wells III, W., 2010. Anatomical atlas-guided diffuse optical tomography of brain activation. Neuroimage 49, 561–567.

D'Andrea, C., Comelli, D., Pifferi, A., Torricelli, A., Valentini, G., Cubeddu, R., 2003. Time-resolved optical imaging through turbid media using a fast data acquisition system based on a gated CCD camera. J Phys D: Appl. Phys. 36, 1675-1681.

Dehaes, M., Gagnon, L., Lesage, F., Pelegrini-Issac, M., Vignaud, A., Valabregue, R., Grebe, R., Wallois, F., Benali, H., 2011a. Quantitative investigation of the effect of the extra-cerebral vasculature in diffuse optical imaging: a simulation study. Biomedical Optics Express 2(3), 680-695.

Formatted: Font: Not Bold, Italian (Italy)

Formatted: Font: Not Bold, Italian (Italy)

Formatted: Font: Not Bold, Italian (Italy)

Formatted: Italian (Italy)

Formatted: Font: Not Bold, Italian (Italy)

Formatted: Font: Not Bold, Italian (Italy)

Formatted: Font: Not Bold, Italian (Italy)

Formatted: Font: Not Bold, Italian (Italy)

Formatted: Italian (Italy)

Formatted: Font: Not Bold, Italian (Italy)

Formatted: Font: Not Bold, Italian (Italy)

Formatted: Font: Not Bold, Italian (Italy)

Dehaes, M., Grant, P.E., Sliva, D.D., Roche-Labarbe, N., Pienaar, R., Boas, D.A., Franceschini, M.A., Selb, J., 2011b. Assessment of the frequency-domain multi-distance method to evaluate the brain optical properties: Monte Carlo simulations from neonate to adult. Biomed Opt Express 2(3), 552-567.

Del Bianco, S., Martelli, F., Zaccanti, G., 2002. Penetration depth of light re-emitted by a diffusive medium: theoretical and experimental investigation. Phys. Med. Biol. 47, 4131–4144.

Del Bianco, S., Martelli, F., Cignini, F., Zaccanti, G., Sansone, G., Pifferi, A., Torricelli, A., Bassi, A., Taroni, P., Cubeddu, R., 2004. Liquid phantom for investigating light propagation through layered diffusive media, Opt. Express. 12, 2102-2111.

Delpy, D.T., Cope, M., van der Zee, P., Arridge, S., Wray, S., Wyatt, J., 1988. Estimation of optical pathlength through tissue from direct time of flight measurement. Phys. Med. Biol. 33, 1433–1442.

Diop, M., St Lawrence, K., 2012. Deconvolution method for recovering the photon time-of-flight distribution from time-resolved measurements. Opt Lett. 37(12), 2358-2360.

Diop, M., Tichauer, K.M., Elliott, J.T., Migueis, M., Lee, T.Y., St Lawrence. K., 2010. Comparison of time-resolved and continuous-wave near-infrared techniques for measuring cerebral blood flow in piglets. J. Biomed. Opt. 15(5), 057004.

Diop, M., Verdecchia, K., Lee, T., St Lawrence, K., 2011. Calibration of diffuse correlation spectroscopy with a time-resolved near-infrared technique to yield absolute cerebral blood flow measurements. Biomedical Optics Express 2(7), 2068-2082.

Dunn, A.K., Boas, D.A., 2000. Transport-based image reconstruction in turbid media with small source–detector separations. Opt. Lett. 25 (24), 1777–1779.

Durduran, T., Choe, R., Baker, W.B., Yodh, A.G., 2010. Diffuse optics for tissue monitoring and tomography. Rep. Prog. Phys. 73, 076701 (43pp).

Eda, H., Oda, I., Ito, Y., Wada, Y., Oikawa, Y., Tsunazawa, Y., Takada, M., Tsuchiya, Y., Yamashita, Y., Oda,M., Sassaroli, A., Yamada, Y., Tamura,M., 1999. Multichannel timeresolved optical tomographic imaging system. Rev. Sci. Instrum. 70, 3595–3602.

Edinburgh Photonics, 2013. The EPL Series, Picosecond Pulsed Diode Lasers. http://www.edinburghphotonics.com/files/file/technical-specifications/EPL%20Series%20Flyer.pdf

Eggebrecht, A.T., White, B.R., Ferradal, S.L., Chen, C., Zhan, Y., Snyder, A.Z., Dehghani, H., Culver, J.P., 2012. A quantitative spatial comparison of high-density diffuse optical tomography and fMRI cortical mapping. NeuroImage. 61(4), 1120-1128.

Formatted: Font: Not Bold, Italian (Italy)

Formatted: Italian (Italy)

Formatted: Font: Not Bold, Italian (Italy)

Formatted: Font: Not Bold, Italian (Italy)

Formatted: Font: Not Bold, Italian (Italy)

Formatted: Italian (Italy)

Formatted: Font: Not Bold, Italian (Italy)

Eggleton, B.J., Luther-Davies, B., Richardson, K., 2011. Chalcogenide photonics. Nature Photonics. 5, 141–148.

Enfield, L.C., Gibson, A.P., Everdell, N.L., Delpy, D.T., Schweiger, M., Arridge, S.R., Richardson, C., Keshtgar, M., Douek, M., Hebden, J.C., 2007. Three-dimensional time-resolved optical mammography of the uncompressed breast. Appl. Opt. 46, 3628-3638.

Excelitas Technologies Corp, 2013. Single Photon Counting Modules. http://www.excelitas.com/Pages/Product/Single-Photon-Counting-Modules-SPCM.aspx

Fang , Q., Boas, D.A., 2009. Monte Carlo Simulation of Photon Migration in 3D Turbid Media Accelerated by Graphics Processing Units. Opt. Express 17(22), 20178-20190.

Fang, Q., 2010. Mesh-based Monte Carlo method using fast ray-tracing in Plücker coordinates. Biomed. Opt. Express 1(1), 165-175.

Fang, Q., Kaeli, D.R., 2012. Accelerating mesh-based Monte Carlo method on modern CPU architectures. Biomed. Opt. Express 3(12), 3223-3230.

Fang, Z., Zhao, C.Z., 2012. Recent Progress in Silicon Photonics: A Review. ISRN Optics 2012 (2012), Article ID 428690.

Farina, A., Bassi, A., Pifferi, A., Taroni, P., Comelli, D., Spinelli, L., Cubeddu, R., 2009. Bandpass effects in time-resolved diffuse spectroscopy. applied spectroscopy. 63(1), 48-56.

Feng, S., Zeng, F., Chance, B., 1995. Photon migration in the presence of a single defect: a perturbation analysis. Appl. Opt. 34(19), 3826-3837.

Ferrari, M., De Blasi, R.A., Safoue, F., Wei, Q., Zaccanti, G., 1993. Towards human brain near infrared imaging: time resolved and unresolved spectroscopy during hypoxic hypoxia. Adv. Exp. Med. Biol. 333, 21–31.

Ferrari, M., Norris, K.H., Sowa, M.G., (Eds.), 2012. Medical Applications of NIR spectroscopy. J. Near Infrared Spectrosc. Volume 20 Issue 1.

Ferrari, M., Quaresima, V., 2012. A brief review on the history of human functional near-infrared spectroscopy (fNIRS) development and fields of application, NeuroImage 63, 921–935.

Fianium UK Ltd., 2013a. ALP (advanced laser platform). http://www.fianium.com/alp.htm.

Fianium UK Ltd., 2013b. WhiteLAse SC sources and accessories. http://www.fianium.com/supercontinuum.htm.

Formatted: Font: Not Bold, Italian (Italy)

Formatted: Italian (Italy)

Formatted: Font: Not Bold, Italian (Italy)

Formatted: Font: Not Bold, Italian (Italy)

Formatted: Italian (Italy)

Formatted: Font: Not Bold, Italian (Italy)

Foschum, F., Fugger, O., Jäger, M., Simon, E., Kienle, A., Pifferi, A., Spinelli, L., Torricelli, A., Farina, A., Bargigia, I., Cubeddu, R., Jelzow, A., Wabnitz, H., Macdonald, R., Martelli, F., Zaccanti, G., Heiskala, J., Arridge, S.R., Liebert, A., Sawosz, P., Milej,D., 2012. In vivo optical spectroscopy of the head. Oral communication to the nEUROPt Workshop, Non-invasive imaging of brain function and disease by pulsed near infrared light, Milan, 12-13 March 2012.

Frederick, B., Boas, D.A., 2013. http://fnirs.org/software/.

Fujimoto, J.G., Brezinski, M.E., Tearney, G.J., Boppart, S.A., Bouma, B.E., Hee, M.R., Southern, J.F., Swanson, E.A.,1995. Optical biopsy and imaging using optical coherence tomography. Nat. Methods 1, 970–972.

Fukui, Y., Ajichi, Y., Okada, E ., 2003. Monte carlo prediction of near-infrared light propagation in realistic adult and neonatal head models. Appl. Opt. 42, 2881–2887.

Gagnon, L., Cooper, R.J., Yucel, M.A., Perdue, K.L., Greve, D.N. and Boas, D.A., 2012a. Short separation channel location impacts the performance of short channel regression in NIRS. Neuroimage 59: 2518–2528.

Gagnon, L., Gauthier, C., Hoge, R.D., Lesage, F., 2008. Double-layer estimation of intra- and extracerebral hemoglobin concentration with a time-resolved system, J. Biomed. Opt., 13(5), 054019.

Gagnon, L., Yucel, M.A., Dehaes, M., Cooper, R.J., Perdue, K.L., Selb, J., Huppert, T.J., Hoge, R.D. and Boas, D.A., 2012b. Quantification of the cortical contribution to the NIRS signal over the motor cortex using concurrent NIRS-fMRI measurements. Neuroimage 59, 3933-3940.

Gao, F., Zhao, H., Tanikawa, Y., Yamada, Y., 2004. Optical tomographic mapping of cerebral haemodynamics by means of time-domain detection: methodology and phantom validation. Phys. Med. Biol. 49 (2004) 1055–1078.

Gerega, A., Milej, D., Weigl, W., Botwicz, M., Zolek, N., Kacprzak, M., Wierzejski, W., Toczylowska, B., Mayzner-Zawadzka, E., Maniewski, R., Liebert, A., 2012. Multiwavelength time-resolved detection of fluorescence during the inflow of indocyanine green into the adult's brain. J. Biomed. Opt. 17(8), 87001.

Gervain, J., Mehler, J., Werker, J.F., Nelson, C.A., Csibra, G., Lloyd-Fox, S., Shukla, M., Aslin, R.A., 2011. Near-infrared spectroscopy: a report from the McDonnell infant methodology consortium. Dev. Cogn. Neurosci. 1, 22–46.

Formatted: Font: Not Bold, Italian (Italy)

Formatted: French (France)

Formatted: French (France)

Formatted: Font: Not Bold, French (France)

Formatted: Font: Not Bold, English (U.K.)

Formatted: English (U.K.)

Formatted: Font: Not Bold, English (U.K.)

Gibson, A.P., Austin, T., Everdel, N.L., Schweiger, M., Arridge, S.R., Meek, J.H., Wyatt, J.S., Delpy, D.T., Hebden, J.C., 2006. Three-dimensional whole-head optical tomography of passive motor evoked responses. NeuroImage 30, 521–528.

Golovko, D., Meier, R., Rummeny, E., Daldrup-Link, H., 2011. Optical imaging of rheumatoid arthritis. Int J Clin Rheumtol. 6(1): 67–75.

Gowar, J., 1993. Optical Communication Systems 2nd edition. Prentice Hall, Hemel Hempstead.

Hamamatsu Photonics, K.K., 2013a. Guide to streak camera. http://sales.hamamatsu.com/assets/pdf/catsandguides/e_streakh.pdf.

Hamamatsu Photonics, K.K., 2013b. Microchannel Plates. http://sales.hamamatsu.com/en/products/electron-tube-division/detectors/microchannel-plates-mcps.php.

Hamamatsu Photonics, K.K., 2013c. Photomultiplier Modules. http://sales.hamamatsu.com/en/products/electron-tube-division/detectors/photomultiplier-modules.php.

Hamamatsu Photonics, K.K., 2013d. Picosecond light pulser. http://sales.hamamatsu.com/assets/pdf/hpspdf/e_plp10.pd.f

Hamamatsu Photonics, K.K., 2013e. TRS-20 http://jp.hamamatsu.com/products/life-science/1002/index_en.html.

Hebden, J.C., Gonzalez, F.M., Gibson, A., Hillman, E.M.C., Yusof, R.M., Everdell, N., Delpy, D.T., Zaccanti, G., Martelli, F., 2003. Assessment of an in situ temporal calibration method for time-resolved optical tomography. J. Biomed. Opt. 8(1), 87–92.

Hebden, J.C., Gibson, A.P., Austin, T., Yusof, R.M., Everdell, N., Delpy, D.T., Arridge, S.R., Meek, J.H., Wyatt, J.S., 2004. Imaging changes in blood volume and oxygenation in the newborn infant brain using three-dimensional optical tomography. Phys. Med. Biol. 49 (7), 1117– 1130.

Hebden, J.C., Magazov, S., Everdell, N., Varela, M., 2012a. A time-domain system for optical tomography of the newborn infant brain. Oral communication to the nEUROPt Workshop, Non-invasive imaging of brain function and disease by pulsed near infrared light, Milan, 12-13 March 2012.

Hebden, J.C., Varela, M., Magazov, S., Everdell, N., Gibson, A., Meek, J., Austin, T., 2012b. Diffuse optical imaging of the newborn infant brain. Proc. of 9th IEEE International Symposium, "Biomedical Imaging: from Nano to Macro", 2-5 May 2012 (Barcelona).

Hervé L., Puszka A., Planat-Chrétien A., Dinten J.M., 2012. Time-domain diffuse optical tomography processing by using the Mellin-Laplace transform. Appl Opt. 51(25), 5978-5988.

Formatted: Font: Not Bold, French (France)

Formatted: French (France)

Formatted: Font: Not Bold, French (France)

Formatted: French (France)

Formatted: Font: Not Bold, French (France)

Formatted: Font: Not Bold, German (Germany)

Hielscher, A.H., Kim, H.K., Klose, A.H., 2011. Forward models of light transport in biological tissue. In Handbook of Biomedical Optics, Part III, Chap. 16. Boas, D.A., Pitris, C., Ramanujam, N., (Eds.) CRC Press Boca Raton, Florida.

Hielscher, A.H., Klose, A.D., Beuthan, J., 2000. Evolution strategies for optical tomography characterization of homogeneous media. Opt. Express 7, 507-518.

Hillman, E.M.C., Amoozegar, C.B., Wang, T., McCaslin, A.F.H., Bouchard, M.B., Mansfield, J., Levenson, R.M., 2011. In vivo optical imaging and dynamic contrast methods for biomedical research Phil. Trans. R. Soc. A 369, 4620-4643.

Hillman, E.M.C., Boas, D.A., Dale, A.M., Dunn, A.K., 2004. Laminar optical tomography: demonstration of millimeter-scale depth-resolved imaging in turbid media. Opt. Lett. 29 (14), 1650–1652.

Hintz, S.R., Benaron, D.A., van Houten, J.C., Duckworth, J.L., Liu, F.W.H., Spilman, S.D., Stevenson, D.K., Cheong, W., 1998. Stationary Headband for Clinical Time-of-Flight Optical Imaging at the Bedside. Photochem. Photobiol. 68(3), 361–369.

Ho, P.P., Baldeck, P., Wong, K.S., Yoo, K.M., Lee, D., Alfano, R.R., 1989. Time dynamics of photon migration in semiopaque random media. Appl. Opt. 28:2304-2310.

Hoshi, Y., Shinba, T., Sato, C., Doi, N., 2006. Resting hypofrontality in schizophrenia: A study using near-infrared time-resolved spectroscopy. Schizophrenia Research 84, 411 – 420.

Hwang, J., Ramella-Roman, J., Nordstrom, R., 2012. Introduction: Feature issue on phantoms for the performance evaluation and validation of optical medical imaging devices. Biomed. Opt. Expr. 3, 1399–403.

ID Quantique SA, 2013. id100 SERIES. http://www.idquantique.com/instrumentation/product/id100-silicon-apd-single-photon-detector.html.

Ijichi, S., Kusaka, T., Isobe, K., Islam, F., Okubo, K., Okada, H., Namba, M., Kawada, K., Imai, T., Itoh, S., 2005a. Quantification of cerebral hemoglobin as a function of oxygenation using near-infrared time-resolved spectroscopy in a piglet model of hypoxia. J. Biomed. Opt. 10(2), 024026.

Ijichi, S., Kusaka, T., Isobe, K., Okubo, K., Kawada, K., Namba, M., Okada, H., Nishida, T., Imai, T., Itoh, S., 2005b. Developmental Changes of Optical Properties in Neonates Determined by Near-Infrared Time-Resolved Spectroscopy. Pediatric Research 58(3), 568-573.

Formatted: Font: Not Bold, German (Germany)

Formatted: English (U.K.)

Formatted: Font: Not Bold, English (U.K.)

Formatted: Font: Not Bold

Formatted: Font: Not Bold, Italian (Italy)

Formatted: Font: Not Bold, French (France)

Formatted: Font: Not Bold, French (France)

Formatted: French (France)

Formatted: Font: Not Bold, French (France)

Formatted: French (France)

Formatted: Font: Not Bold, French (France)

Ijichi, S., Kusaka, T., Isobe, K., Okubo, K., Yasuda, S., Kawada K., Itoh S., 2005c. Developmental changes of optical properties in infants determined by near-infrared time-resolved spectroscopy. J. Cereb. Blood Flow Metab. 25, S228

International Electrotechnical Commission, 2001. IEC 60825-1, Edition 1.2. Safety of laser products - Part 1: Equipment classification, requirements and user's guide.

International Electrotechnical Commission, 2013. IEC 80601-2-71 Ed. 1.0. Medical electrical equipment - Part 2-71: Particular requirements for the basic safety and essential performance of functional oximeter equipment. http://www.iec.ch/dyn/www/f?p=103:38:0::::FSP_ORG_ID,FSP_APEX_PAGE,FSP_LANG_ID,FSP_PROJECT:1365,23,25,IEC%2080601-2-71%20Ed.%201.0

Intes, X., 2005. Time-domain optical mammography SoftScan: Initial results. Acad. Radiol. 12: 934-947.

Jacques, S.L., 1989a. Time resolved propagation of ultrashort laser pulses within turbid tissues. Appl. Opt. 28:2223-2239.

Jacques, S.L., 1989b. Time-resolved reflectance spectroscopy in turbid tissues. IEEE Trans. Biomed. Eng. 36:1155-1161.

Jelzow, A., Kirilina, E., Wabnitz, H., Kummrow, A., Bruehl, R., Ittermann, B., Macdonald, R., 2009. Towards improved quantification of functional activation in human brain by concurrent fMRI and time-resolved NIRS. 446. WE-Heraeus-Seminar "Optical Imaging of Brain Function" December 7th-10th, 2009, Bad Honnef, Germany.

Jelzow, A., Koch, S., Wabnitz, H., Steinbrink, J., Obrig, H., Macdonald, R., 2010. Combined EEG and time-resolved NIRS to study neurovascular coupling in the adult brain. International Summer School on Multimodal Approaches in Neuroscience July 19th-21st, 2010 (Leipzig, Germany).

Jelzow, A., Wabnitz, H., Obrig, H., Macdonald, R., Steinbrink, J., 2012. Separation of indocyanine green boluses in the human brain and scalp based on time-resolved in-vivo fluorescence measurements. J. Biomed. Opt. 17(5), 057003.

Kacprzak, M., Liebert, A., Sawosz, P., Zolek, N., Maniewski, R., 2007. Time-resolved optical imager for assessment of cerebral oxygenation. J. Biomed. Opt. 12, 034019.

Kacprzak, M., Liebert, A., Staszkiewicz, W., Gabrusiewicz, A., Sawosz, P., Madycki, G., Maniewski, R., 2012. Application of a time-resolved optical brain imager for monitoring cerebral oxygenation during carotid surgery. J. Biomed. Opt. 17(1), 016002.

Formatted: Font: Not Bold, German (Germany)

Formatted: Font: Not Bold, German (Germany)

Kakihana, Y., Kiyonaga, N., Yasuda, T., Imabayashi, T., Ohryoji, T., Nakahara, M., Okayama, N., Kanmura, Y., Kikuchi, T., Yonemitsu, T., 2010. Dynamic changes in cerebral oxygenation by two methods during cardiac surgery and postoperative cognitive decline. Crit Care. 2010; 14(Suppl 1): P334.

Kakihana, Y., Okayama, N., Matsunaga, A., Yasuda, T., Imabayashi, T., Nakahara, M., Kiyonaga, N., Ikoma, K., Kikuchi, T., Kanmura, Y., Oda, M., Ohmae, E., Suzuki, T., Yamashita, Y., Tamura, M., 2012. Cerebral Monitoring Using Near-Infrared Time-Resolved Spectroscopy and Postoperative Cognitive Dysfunction. Adv. Exp. Med. Biol. 737, 19-24.

Kiguchi, M., Ichikawa, N., Atsumori, H., Kawaguchi, F., Sato, H., Maki, A., Koizumi, H., 2007. Comparison of light intensity on the brain surface due to laser exposure during optical topography and solar irradiation. J. Biomed. Opt. 12(6), 062108.

Kirilina, E., Jelzow, A., Heine, A., Niessing, M., Wabnitz, H., Brühl, R., Ittermann, B., Jacobs, A.M., Tachtsidis, I.,2012. The physiological origin of task-evoked systemic artefacts in functional near infrared spectroscopy. NeuroImage. 61(1), 70-81.

Kuga, Y., Ishimaru, A., and Bruckner, A. P. 1983. Experiments on picosecond pulse propagation in a diffuse medium, J. Opt. Soc. Am. A 73:1812-1815.

Lapointe, E., Pichette, J., Bérubé-Lauzière, Y., 2012. A multi-view time-domain non-contact diffuse optical tomography scanner with dual wavelength detection for intrinsic and fluorescence small animal imaging. Rev. Sci. Instrum. 83, 063703 (2012).

LaVision BioTec GmbH, 2013. Ultra-Fast Gated Cameras. http://www.lavision.de/products/cameras/ultrafast_gated_cameras.php.

Liebert, A., Sawosz, P., Milej, D., Kacprzak, M., Weigl, W., Botwicz, M., Mączewska, J., Fronczewska, K., Mayzner-Zawadzka, E., Królicki, L., Maniewski, R., 2011. Assessment of inflow and washout of indocyanine green in the adult human brain by monitoring of diffuse reflectance at large source-detector separation. J. Biomed. Opt. 16(4), 046011.

Liebert, A., Wabnitz, H., Elster C., 2012. Determination of absorption changes from moments of distributions of times of flight of photons: optimization of measurement conditions for a two-layered tissue model. J. Biomed. Opt. 17(5), 057005.

Liebert, A., Wabnitz, H., Grosenick, D., Macdonald, R., 2003. Fiber dispersion in time domain measurements compromising the accuracy of determination of optical properties of strongly scattering media. J. Biomed. Opt. 8(3), 512-516.

Formatted: Font: Not Bold, German (Germany)

Formatted: German (Germany)

Liebert, A., Wabnitz, H., Obrig, H., Erdmann, R., Möller, M., Macdonald, R., Rinneberg, H., Villringer, A., Steinbrink, J., 2006. Non-invasive detection of fluorescence from exogenous chromophores in the adult human brain. NeuroImage. 31(2), 600-608.

Liebert, A., Wabnitz, H., Steinbrink, J., Möller, M., Macdonald, R., Rinneberg, H., Villringer, A., Obrig, H., 2005. Bed-side assessment of cerebral perfusion in stroke patients based on optical monitoring of a dye bolus by time-resolved diffuse reflectance. NeuroImage, Volume 24(2), 426-435.

Liebert, A., Wabnitz, H., Steinbrink, J., Obrig, H., Möller, M., Macdonald, R., Villringer, A., Rinneberg, H., 2004. Time-resolved multidistance near-infrared spectroscopy of the adult head: intracerebral and extracerebral absorption changes from moments of distribution of times of flight of photons. Appl Opt. 43(15), 3037-3047.

Liemert, A., Kienle, A., 2012. Green's function of the time-dependent radiative transport equation in terms of rotated spherical harmonics. Phys. Rev. E 86, 036603.

Liu, Y., Zhang, X., 2011. Metamaterials: a new frontier of science and technology. Chem. Soc. Rev. 40, 2494-2507.

Maas, A.I.R., Citerio, G., 2010. Noninvasive monitoring of cerebral oxygenation in traumatic brain injury: a mix of doubts and hope. Intensive Care Med. 36, 1283-1285.

Mackert, B., Leistner, S., Tilmann Sander, Liebert, A., Wabnitz, H., Burghoff, M., Trahms, L., Macdonald, R., Curio, G., 2008. Dynamics of cortical neurovascular coupling analyzed by simultaneous DC-magnetoencephalography and time-resolved near-infrared spectroscopy. NeuroImage. 39(3), 979-986.

Martelli, F., Del Bianco, S., Ismaelli, A., Zaccanti, G., 2009. Light Propagation through Biological Tissue and Other Diffusive Media: Theory, Solutions, and Software, Washington, USA, SPIE Press.

Martelli, F., Del Bianco, S., Zaccanti G., 2003. Procedure for retrieving the optical properties of a two-layered medium from time-resolved reflectance measurements. Opt. Lett. 28(14), 1236-1238.

Martelli, F., Del Bianco, S., Zaccanti G., Pifferi, A., Torricelli, A., Bassi, A., Taroni, P., Cubeddu, R., 2004. Phantom validation and in vivo application of an inversion procedure for retrieving the optical properties of diffusive layered media from time-resolved reflectance measurements. Opt. Lett. 29(17), 2037-2039.

Martelli, F., Del Bianco, S., Zaccanti, G., 2012. Retrieval procedure for time-resolved near-infrared tissue spectroscopy based on the optimal estimation method. Phys Med Biol. 2012 May 21;57(10):2915-29.

Formatted: Font: Not Bold, German (Germany)

Formatted: Font: Not Bold, German (Germany)

Formatted: German (Germany)

Formatted: Font: Not Bold, German (Germany)

Formatted: Font: Not Bold, German (Germany)

Formatted: German (Germany)

Formatted: Font: Not Bold, German (Germany)

Formatted: Font: Not Bold, German (Germany)

Formatted: German (Germany)

Formatted: Font: Not Bold, German (Germany)

Formatted: Font: Not Bold, Italian (Italy)

Formatted: Italian (Italy)

Formatted: Font: Not Bold, Italian (Italy)

Formatted: Font: Not Bold, Italian (Italy)

Formatted: Font: Not Bold, Italian (Italy)

Formatted: Italian (Italy)

Formatted: Font: Not Bold, Italian (Italy)

Mata Pavia, J., Niclass, C., Favi, C., Wolf, M., Charbon, E., 2011a. 3D near-infrared imaging based on a SPAD image sensor. In: International Image Sensor Workshop (IISW), Hokkaido, Japan, 08 June 2011 - 11 June 2011, R42.

Mata Pavia,J., Charbon, E., Wolf, M., 2011b, 3D near-infrared imaging based on a single-photon avalanche diode array sensor. Proc. SPIE 8088, 808811.

Mata Pavia,J., Charbon, E., Wolf, M., 2012. 3D near-infrared imaging based on a single-photon avalanche diode array sensor: A new perspective on reconstruction algorithms. Conference Paper, Biomedical Optics, Miami, Florida, April 28, 2012, Nevel Techniques and Models (BW1A), BW1A.5.

Mazurenka, M., Di Sieno, L., Boso, G., Contini, D., Pifferi, A., Dalla Mora, A., Tosi, A., Wabnitz, H., Macdonald, R., 2013. Development of an optical non-contact time-resolved diffuse reflectance scanning imaging system: first in vivo tests. Oral communication at SPIE BiOS 2013 Conference 8578 Optical Tomography and Spectroscopy of Tissue X, 6 February 2013, Paper 8578-88.

Mazurenka, M., Jelzow, A., Wabnitz, H., Contini, D., Spinelli, L., Pifferi, A., Cubeddu, R., Dalla Mora, A., Tosi, A., Zappa, F., Macdonald, R., 2012. Non-contact time-resolved diffuse reflectance imaging at null source-detector separation, Opt. Express 20(1), 283-290.

MCML, 2013. http://omlc.ogi.edu/software/mc/.

Micro Photon Devices, 2013a. PDM series. http://www.micro-photon-devices.com/products_pdm.asp.

Micro Photon Devices, 2013b. PDM-R series. http://www.micro-photon-devices.com/products_pdm-r.asp

Micro Photon Devices, 2013c. SPC2 series. http://www.micro-photon-devices.com/products_spc2.asp

Milej, D., Gerega, A., Zołek, N., Weigl, W., Kacprzak, M., Sawosz, P., Mączewska, J., Fronczewska, K., Mayzner-Zawadzka, E., Królicki, L., Maniewski, R., Liebert ,A., 2012. Time-resolved detection of fluorescent light during inflow of ICG to the brain-a methodological study. Phys Med Biol. 57(20), 6725-6742.

Molteni, E., Contini, D., Caffini, M., Baselli, G., Spinelli, L., Cubeddu, R., Cerutti, S., Bianchi, A.M., Torricelli, A., 2012. Load-dependent brain activation assessed by time-domain functional near-infrared spectroscopy during a working memory task with graded levels of difficulty. J. Biomed. Opt. 17 (5), 056005.

Montcel, B., Chabrier, R., Poulet, P., 2005. Detection of cortical activation with time-resolved diffuse optical methods. Appl. Opt. 44(10), 1942-1947.

Formatted: Font: Not Bold, Italian (Italy)

Formatted: Font: Not Bold, Italian (Italy)

Formatted: Font: Not Bold, French (France)

Formatted: French (France)

Formatted: Font: Not Bold, French (France)

Formatted: French (France)

Formatted: Font: Not Bold, French (France)

Formatted: French (France)

Formatted: Font: Not Bold, French (France)

Formatted: French (France)

Formatted: Font: Not Bold, French (France)

Formatted: Font: Not Bold, Italian (Italy)

Formatted: Italian (Italy)

Formatted: Font: Not Bold, Italian (Italy)

Montcel, B., Chabrier, R., Poulet, P., 2006. Time-resolved absorption and hemoglobin concentration difference maps: a method to retrieve depth-related information on cerebral hemodynamics. Opt. Expr. 14(25), 12271- 12287.

Montcel, B., Poulet, P., 2006. An instrument for small-animal imaging using time-resolved diffuse and fluorescence optical methods. Nuclear Instruments and Methods in Physics Research Section A: Accelerators, Spectrometers, Detectors and Associated Equipment. 569(2), 551–556.

Moreira-Gonzalez, A., Papay, F.E., Zins, J.E., 2006. Calvarial thickness and its relation to cranial bone harvest. Plast Reconstr Surg. 117(6), 1964-1971.

Mottin, S., Montcel, B., de Chatellus, H.G., Ramstein, S., 2011. Functional white-laser imaging to study brain oxygen uncoupling/recoupling in songbirds. J. Cereb. Blood Flow Metab. 31(2), 393-400.

Newport Corporation, 2013. Ultrafast Lasers. http://www.newport.com/Ultrafast-Lasers/989320/1033/content.aspx.

Niedre, M.J., Turner, G.M., Ntziachristos, V., 2006. Time-resolved imaging of optical coefficients through murine chest cavities, J. Biomed. Opt. 11(1), 064017.

Ntziachristos, V., Ma, X., Yodh, A.G., Chance, B., 1999. Multichannel photon counting instrument for spatially resolved near infrared spectroscopy. Rev. Sci. Instrum. 70(1), 193-201.

NIRFAST, 2013. http://www.dartmouth.edu/~nir/nirfast/.

NKT Photonics, 2013a. Large Mode Area (LMA) fibers. http://www.nktphotonics.com/lmafibers-specifications.

NKT Photonics, 2013b. SuperK Supercontinuum sources. http://www.nktphotonics.com/supercontinuum_sources.

Nomura, Y., Hazekiy, O., Tamura M., 1997. Relationship between time-resolved and non-time-resolved Beer–Lambert law in turbid media. Phys. Med. Biol. 42, 1009–1022.

O'Connor, D.V., Phillips, D., 1984. Time correlated single photon counting, Academic Press, London.

Obrig, H., Hirth, C., Ruben, J., Dirnagl, U., Villringer, A., Wabnitz, H., Grosenick, D.,Rinneberg, H., 1996. Near-infrared spectroscopy in functional activation studies: new approaches. NeuroImage 3 (Suppl. 1), S 403.

Oda, M., Ohmae, E., Suzuki, H., Suzuki, T., Yamashita, Y., 2009. Tissue oxygenation measurements using near-infrared time-resolved spectroscopy. J. Jpn. Coll. Angiol. 49, 131–137.

Formatted: Font: Not Bold, German (Germany)

Formatted: German (Germany)

Formatted: Font: Not Bold, German (Germany)

Formatted: Font: (Default) Times New Roman, 11 pt, Not Bold, Font color: Custom Color(RGB(84;141;212))

Formatted: German (Germany)

Formatted: Font: Not Bold, German (Germany)

Formatted: Font: Not Bold, Italian (Italy)

Oda, M., Yamashita, Y., Nakano, T., Suzuki, A., Shimizu, K., Hirano, I., Shimomura, F., Ohmae, E., Suzuki, T., Tsuchiya, Y., 1999. Near infrared time-resolved spectroscopy system for tissue oxygenation monitor. Proc. SPIE 3597, 611–617.

Ohmae, E., Oda, M., Suzuki, T., Yamashita, Y., Kakihana, Y., Matsunaga, A., Kanmura, Y., Tamura, M., 2007. Clinical evaluation of time-resolved spectroscopy by measuring cerebral hemodynamics during cardiopulmonary bypass surgery. J. Biomed. Opt. 12(6), 062112.

Ohmae, E., Ouchi, Y., Oda, M., Suzuki, T., Nobesawa, S., Kanno, T., Yoshikawa, E., Futatsubashi, M., Ueda, Y., Okada, H., Yamashita, Y., 2006. Cerebral hemodynamics evaluation by near-infrared time-resolved spectroscopy: correlation with simultaneous positron emission tomography measurements. NeuroImage 29, 697–705.

Okamoto, M., Dan, H., Sakamoto, K., Takeo, K., Shimizu, K., Kohno, S., Oda, I., Isobe, S., Suzuki, T., Kohyama, K., Dan, I., 2004. Three-dimensional probabilistic anatomical cranio-cerebral correlation via the international 10–20 system oriented for transcranial functional brain mapping. NeuroImage 21, 99–111.

Patterson, M.S., Chance, B., Wilson, B.C., 1989. Time resolved reflectance and transmittance for the non-invasive measurement of tissue optical properties. Appl. Opt. 28:2331-2336.

PicoQuant GmbH, 2013a. Hybrid Photomultiplier Detector Assembly. http://www.picoquant.com/products/hpd/hpd.htm.

PicoQuant GmbH, 2013b. LDH Series. http://www.picoquant.com/products/ldh/ldhseries.htm.

PicoQuant GmbH, 2013c. LDH-FA Series. http://www.picoquant.de/products/ldh_fa/ldh-fa.htm.

PicoQuant GmbH, 2013d. Multichannel Picosecond Event Timer & TCSPC Module. http://www.picoquant.com/products/hydraharp400/hydraharp400.htm.

PicoQuant GmbH, 2013e. Single Photon Counting Module. http://www.picoquant.com/products/tau_spad/tau_spad.htm.

Pifferi, A., Contini, D., Spinelli, L., Torricelli, A., Cubeddu, R., Martelli, F., Zaccanti, G., Dalla Mora, A., Tosi, A., Zappa, F., 2010. The spread matrix: a method to predict the effect of a non time-invariant measurement system. Biomedical Optics, OSA Technical Digest (CD), Optical Society of America. paper BSuD22, page 1-3.

Pifferi, A., Torricelli, A., Bassi, A., Taroni, P., Cubeddu, R., Wabnitz, H., Grosenick, D., Möller, M., MacDonald, R., Swartling, J., Svensson, T., Andersson-Engels, S., van Veen, R.L.P., Sterenborg,

Formatted: Font: Not Bold, German (Germany)

Formatted: German (Germany)

Formatted: Font: Not Bold, German (Germany)

Formatted: Font: Not Bold, Italian (Italy)

Formatted: Italian (Italy)

Formatted: Font: Not Bold

Formatted: Font: Not Bold

Formatted: Font: Not Bold, Italian (Italy)

H.J.C.M., Tualle, J., Nghiem, H.L., Avrillier, S., Whelan, M., Stamm, H., 2005. Performance assessment of photon migration instruments: the MEDPHOT protocol. Appl. Opt. 44, 2104–2114.

Pifferi, A., Torricelli, A., Spinelli, L., Contini, D., Cubeddu, R., Martelli, F., Zaccanti, G., Tosi, A., Dalla Mora, A., Zappa, F., Cova, S., 2008. Time-resolved diffuse reflectance at null source-detector separation using a fast gated single-photon avalanche diode. Phys. Rev. Lett. 100, 138101.

Pifferi, A., Torricelli, A., Taroni, P., Cubeddu, R., 2001. Reconstruction of absorber concentrations in a two-layer structure by use of multidistance time-resolved reflectance spectroscopy. Opt. Lett. 26(24), 1963-1965.

Prahl, S., 2013. Optical Absorption of Hemoglobin. http://omlc.ogi.edu/spectra/hemoglobin/index.html.

Quaresima, V., Ferrari, M., Torricelli, A., Spinelli, L., Pifferi, A., Cubeddu, R., 2005. Bilateral prefrontal cortex oxygenation responses to a verbal fluency task: a multichannel time-resolved near-infrared topography study. J. Biomed. Opt. 10, 11012.

Re, R., Contini, D., Caffini, M., Cubeddu, R., Spinelli, L., Torricelli, A., 2010. A compact time-resolved system for near infrared spectroscopy based on wavelength space multiplexing. Rev. Sci. Instrum. 81(11), 113101.

Ren, N., Liang, J., Qu, X., Li, J., Lu, B., Tian, J., 2010. GPU-based Monte Carlo simulation for light propagation in complex heterogeneous tissues. Opt. Express 18(7), 6811-6823.

Saager, R.B., Telleri, N.L., Berger, A.J., 2011. Two-detector Corrected Near Infrared Spectroscopy (C-NIRS) detects hemodynamic activation responses more robustly than single-detector NIRS. NeuroImage 55(4), 1679—1685.

Sander, T.H., Liebert, A., Mackert, B.M., Wabnitz, H., Leistner, S., Curio, G., Burghoff, M., Macdonald, R., Trahms, L., 2007. DC-magnetoencephalography and time-resolved near-infrared spectroscopy combined to study neuronal and vascular brain responses. Physiol Meas. 28(6), 651-64

Sassaroli, A., Martelli, F., 2012. Equivalence of four Monte Carlo methods for photon migration in turbid media. JOSA A 29(10), 2110-2117.

Sassaroli, A., Martelli, F., Fantini, S., 2010. Perturbation theory for the diffusion equation by use of the moments of the generalized temporal point-spread function. III. Frequency-domain and time-domain results. JOSA A, 27(7), 1723-1742.

Sato, C., Yamaguchi, T., Seida, M., Ota, Y., Yu, I., Iguchi, Y., Nemoto, M., Hoshi, Y., 2007. Intraoperative monitoring of depth dependent hemoglobin concentration changes during carotid endartectomy by time-resolved spectroscopy. Appl. Opt. 46(14), 2785-2792.

Formatted: Font: Not Bold, Italian (Italy)

Formatted: Font: Not Bold, Italian (Italy)

Formatted: Italian (Italy)

Formatted: Font: Not Bold, Italian (Italy)

Formatted: Font: Not Bold, Italian (Italy)

Formatted: Font: Not Bold, Italian (Italy)

Formatted: Italian (Italy)

Formatted: Font: Not Bold, Italian (Italy)

Formatted: Font: Not Bold, German (Germany)

Formatted: Font: Not Bold, German (Germany)

Formatted: German (Germany)

Formatted: Font: Not Bold, German (Germany)

Sawosz, P., Kacprzak, M., Zolek, N., Weigl, W., Wojtkiewicz, S., Maniewski, R., Liebert., A., 2010. Optical system based on time-gated, intensified charge-coupled device camera for brain imaging studies. J. Biomed. Opt. 15(6), 066025.

Sawosz, P., Zolek, N., Kacprzak, M., Maniewski, R., Liebert A., 2012. Application of time-gated CCD camera with image intensifier in contactless detection of absorbing inclusions buried in optically turbid medium which mimics local changes in oxygenation of the brain tissue. Opto–Electron. Rev., 20(4), 309–314.

Scarpa, F., Brigadoi, S., Cutini, S., Scatturin, P., Zorzi, M., Dell'Acqua, R., Sparacino, G., 2013. A Reference-Channel Based Methodology to Improve Estimation of Event Related Hemodynamic Response from fNIRS Measurements. NeuroImage (in press) doi: 10.1016/j.neuroimage.2013.01.021.

Schmidt, F.E.W.,Fry,M.E.,Hillman,E.M.C., Hebden, J.C., Delpy, D.T.,2000.A32-channel time resolved instrument for medical optical tomography. Rev. Sci. Instrum. 71, 256–265.

Selb, J., Boas, D.A., 2012. A Second Generation Time-Domain Imaging System from MGH, Oral communication to the nEUROPt Workshop, Non-invasive imaging of brain function and disease by pulsed near infrared light, Milan, 12-13 March 2012.

Selb, J., Dale, A., Boas, D.A., 2007. Linear 3D reconstruction of time-domain diffuse optical imaging differential data: improved depth localization and lateral resolution. Opt. Express 15, 16400–16412.

Selb, J., Gibson, A., 2011. Diffuse Optical Tomography : Time Domain. In Handbook of Biomedical Optics, Part III, Chap. 20. Boas, D.A., Pitris, C., Ramanujam, N., (Eds.) CRC Press Boca Raton, Florida.

Selb, J., Joseph, D.K., Boas, D.A., 2006. Time-gated optical system for depth-resolved functional brain imaging. J. Biomed. Opt. 11, 044008.

Selb, J., Stott, J.J., Franceschini, M.A., Sorensen, A.G., Boas, D.A., 2005. Improved sensitivity to cerebral hemodynamics during brain activation with a time-gated optical system: analytical model and experimental validation. J. Biomed. Opt. 10(1), 11013.

Selb, J., Zimmermann, B.B., Martino, M., Ogden, T.M., Boas, D.A., 2013. Functional brain imaging with a supercontinuum time-domain NIRS system. Oral communication at SPIE BiOS 2013 Conference 8578 Optical Tomography and Spectroscopy of Tissue X, 3 February 2013, Paper 8578-7.

SensL, 2013a. Measurement Instruments. http://sensl.com/products/measurement-instruments/.

SensL, 2013b. Photon Counting Systems. http://sensl.com/products/photon-counting-systems/.

Formatted: Font: Not Bold, Italian (Italy)

Formatted: Font: Not Bold, Italian (Italy)

Formatted: Font: Not Bold, Italian (Italy)

Formatted: Italian (Italy)

Formatted: Font: Not Bold, Italian (Italy)

Formatted: Font: Not Bold, Italian (Italy)

Formatted: Font: Not Bold, German (Germany)

Formatted: Font: Not Bold, English (U.K.)

Formatted: Font: Not Bold, English (U.K.)

Formatted: Font: Not Bold

Siesler, H.W., Ozaki, Y., Kawata, S., Heise, H.M., (Eds.), 2002. Near-Infrared Spectroscopy: Principles, Instruments, Apps. Wiley-VCH Verlag GmbH, Weinheim (Germany).

Simon, E., Foschum, F. , Kienle, A., 2013. Hybrid Green's function of the time-dependent radiative transfer equation for anisotropically scattering semi-infinite media. J. Biomed. Opt. 18(1), 015001.

Spinelli, L., Martelli, F., Del Bianco, S., Pifferi, A., Torricelli, A., Cubeddu, R., Zaccanti, G., 2006. Absorption and scattering perturbations in homogeneous and layered diffusive media probed by time-resolved reflectance at null source-detector separation. Phys. Rev. E 74, 021919.

Spinelli, L., Martelli, F., Torricelli, A., Pifferi, A., Zaccanti, G., 2009a. Nonlinear Fitting Procedure for Accurate Time-resolved Measurements in Diffusive Media. Proc SPIE 7369, 73691C.

Spinelli, L., Pifferi, A., Contini, D., Cubeddu, R., Torricelli, A., 2009b. Time-resolved optical stratigraphy in turbid media, Proc SPIE 7371, 73710A.

Steinbrink, J., Wabnitz, H., Obrig, H., Villringer, A., Rinneberg, H., 2001. Determining changes in NIR absorption using a layered model of the human head. Phys. Med. Biol. 46, 879–896.

Steinkellner, O., Gruber, C., Wabnitz, H., Jelzow, A., Steinbrink, J., Fiebach, J.B., Macdonald, R., Obrig, H., 2010. Optical bedside monitoring of cerebral perfusion: technological and methodological advances applied in a study on acute ischemic stroke. J. Biomed. Opt. 15(6), 061708.

Steinkellner, O., Jelzow, A., Wabnitz, H., Macdonald, R., 2012. A time-domain brain imager for various clinical applications. Oral communication to the nEUROPt Workshop, Non-invasive imaging of brain function and disease by pulsed near infrared light, Milan, 12-13 March 2012.

Takahashi, T., Takikawa, Y., Kawagoe, R., Shibuya, S., Iwano, T., Kitazawa, S., 2011. Influence of skin blood flow on near-infrared spectroscopy signals measured on the forehead during a verbal fluency task. NeuroImage 57, 991–1002.

Taroni, P. Pifferi, A., Quarto, G., Spinelli, L., Torricelli, A., Cubeddu, R., 2012. Chapter 9, Diffuse Optical Imaging: Application to Breast Imaging. In *Emerging Imaging Technologies in Medicine*, Anastasio, A., La Riviere, P. (Editors). CRC Press Boca Raton, Florida.

TOAST, 2013. http://web4.cs.ucl.ac.uk/research/vis/toast/index.html.

Tolguenec, G.L., Lantz, E., Devaux, F., 1997. Imaging through scattering media by parametric amplification of images: study of the resolution and the signal-to-noise ratio. Appl. Opt. 36: 8292-8297.

Toninelli, C., Vekris, E., Ozin, G.A., John, S., Wiersma, D.S., 2008. Exceptional Reduction of the Diffusion Constant in Partially Disordered Photonic Crystals. Phys. Rev. Lett. 101, 123901.

Formatted: Font: Not Bold, Italian (Italy)

Formatted: Italian (Italy)

Formatted: Font: Not Bold, Italian (Italy)

Formatted: Font: Not Bold, Italian (Italy)

Formatted: Italian (Italy)

Formatted: Font: Not Bold, Italian (Italy)

Formatted: Font: Not Bold, Italian (Italy)

Formatted: Italian (Italy)

Formatted: Font: Not Bold, Italian (Italy)

Formatted: Font: Not Bold, German (Germany)

Formatted: Font: Not Bold, German (Germany)

Formatted: German (Germany)

Formatted: Font: Not Bold, German (Germany)

Formatted: Font: Not Bold, Italian (Italy)

Formatted: Font: Not Bold, Italian (Italy)

Formatted: Italian (Italy)

Formatted: Font: Not Bold, Italian (Italy)

Formatted: Font: Not Bold, French (France)

Formatted: Font: Not Bold, Italian (Italy)

Formatted: Italian (Italy)

Torricelli, A., Contini, D., Caffini, M., Zucchelli, L., Cubeddu, R., Spinelli, L., Molteni, E., Bianchi, A.M., Baselli, G., Cerutti, S., Visani, E., Gilioli, I., Rossi Sebastiano, D., Schiaffi, E., Panzica, F., Franceschetti, S., 2011. Assessment of cortical response during motor task in adults by a multimodality approach based on fNIRS-EEG, fMRI-EEG, and TMS. Proc SPIE 8088, 808802.

Torricelli, A., Contini, D., Pifferi, A., Spinelli, L., Cubeddu, R., Nocetti, L., Manginelli, A.A., Baraldi, P., 2007. Simultaneous acquisition of time-domain fNIRS and fMRI during motor activity. Proc SPIE 6631, 66310A.

Torricelli, A., Pifferi, A., Spinelli, L., Cubeddu, R., Martelli, F., Del Bianco, S., Zaccanti, G., 2005. Time-Resolved Reflectance at Null Source-Detector Separation: Improving Contrast and Resolution in Diffuse Optical Imaging. Phys. Rev. Lett. 95, 078101.

Torricelli, A., Pifferi, A., Taroni, P., Giambattistelli, E., Cubeddu, R., 2001. In vivo optical characterization of human tissues from 610 to 1010 nm by time-resolved reflectance spectroscopy. Phys. Med. Biol. 46, 2227–2237.

Torricelli, A., Quaresima, V., Pifferi, A., Biscotti, G., Spinelli, L., Taroni, P., Ferrari, M., Cubeddu, R., 2004. Mapping of calf muscle oxygenation and haemoglobin content during dynamic plantar flexion exercise by multi-channel time-resolved near infrared spectroscopy. Phys. Med. Biol. 49, 685–699.

Tosi, A., Dalla Mora, A., Zappa, F., Gulinatti, A., Contini, D., Pifferi, A., Spinelli, L., Torricelli, A., Cubeddu, R., 2011. Fast-gated single-photon counting technique widens dynamic range and speeds up acquisition time in time-resolved measurements. Opt Express 19(11), 10735- 10746.

Tsuzuki, D., Jurcak, V., Singh, A.K., Okamoto, M., Watanabe, E., Dan, I., 2007. Virtual spatial registration of stand-alone fNIRS data to MNI space. Neuroimage. 34(4):1506-18.

Tsuzuki, D., Cai, D.S., Dan, H., Kyutoku, Y., Fujita, A., Watanabe, E., Dan, I., 2012. Stable and convenient spatial registration of stand-alone NIRS data through anchor-based probabilistic registration. Neurosci Res. 72(2), 163-71.

Tuchin, V., 2010. Handbook of Photonics for Biomedical Science, CRC Press, Taylor & Francis Group, London.

Ueda, Y., Yamanaka, T., Yamashita, D., Suzuki, T., Ohmae, E., Oda, M., Yamashita, Y., 2005. Reflectance diffuse optical tomography: its application to human brain mapping. Jpn. J. Appl. Phys. 44, 1203–1206.

van der Zee, P., Cope, M., Arridge, S.R., Essenpreis,M., Potter, L.A., Edwards, A.D.,Wyatt, J.S., McCormick, D.C., Roth, S.C., Reynolds, E.O., 1992. Experimentally measured optical pathlengths for the

Formatted: Font: Not Bold, Italian (Italy)

Formatted: Font: Not Bold, Italian (Italy)

Formatted: Italian (Italy)

Formatted: Font: Not Bold, Italian (Italy)

Formatted: Font: Not Bold, Italian (Italy)

Formatted: Italian (Italy)

Formatted: Font: Not Bold, Italian (Italy)

Formatted: Font: Not Bold, Italian (Italy)

Formatted: Italian (Italy)

Formatted: Font: Not Bold, Italian (Italy)

Formatted: Font: Not Bold, Italian (Italy)

Formatted: Font: Not Bold, Italian (Italy)

Formatted: Font: Not Bold, Italian (Italy)

Formatted: Italian (Italy)

Formatted: Font: Not Bold, Italian (Italy)

adult head, calf and forearm and the head of the newborn infant as a function of inter optode spacing. Adv. Exp. Med. Biol. 316, 143–153.

Vignal, C., Boumans, T., Montcel, B., Ramstein, S., Verhoye, M., Van Audekerke, J., Mathevon, N., Van der Linden, A., Mottin, S., 2008. Measuring brain hemodynamic changes in a songbird: responses to hypercapnia measured with functional MRI and near-infrared spectroscopy. Phys. Med. Biol. 53(10), 2457-70.

Wabnitz, H., Jelzow, A., Mazurenka, M., Steinkellner, O., Taubert, D.R., Macdonald, R., Pifferi, A., Torricelli, A., Contini, D., Zucchelli, L., Spinelli, L., Cubeddu, R., Milej, D., Zolek, N., Kacprzak, M., Sawosz, P., Liebert, A., Magazov, A., Hebden, J.C., Martelli, F., Di Ninni, P., Zaccanti, G., 2013. Performance assessment of time-domain optical brain imagers: a multi-laboratory study. Invited Paper at SPIE BiOS 2013 Conference 8578 Optical Tomography and Spectroscopy of Tissue X, 3 February 2013, Paper 8583-21.

Wabnitz, H., Möller, M., Liebert, A., Walter, A., Erdmann, R., Raitza, O., Drenckhahn, C., Dreier, J., Obrig, H., Steinbrink, J., Macdonald, R., 2005. A time-domain NIR brain imager applied in functional stimulation experiments. Proc. OSA-SPIE Biomed. Opt. Presented at the Photon Migration and Diffuse-Light Imaging II, pp. 70–78.

Wabnitz, H., Möller, M., Liebert, A., Obrig, H., Steinbrink, J., Macdonald, R., 2010. Time-resolved near-infrared spectroscopy and imaging of the adult human brain. Adv. Exp. Med. Biol. 662, 143-148.

Wabnitz, H., Pifferi, A., Torricelli, A., Taubert, D.R., Mazurenka, M., Steinkellner, O., Jelzow, A., Farina, A., Bargigia, I., Contini, D., Caffini, M., Zucchelli, L., Spinelli, L., Sawosz, P., Liebert, A., Macdonald, R., Cubeddu, R. 2011. Assessment of basic instrumental performance of time-domain optical brain imagers. Proc. SPIE. 7896, 789602.

Wang, L., Ho, P.P., Liu, C., Zhang, G., Alfano, R.R., 1991. Ballistic 2-d imaging through scattering walls using an ultrafast optical kerr gate. Science 253, 769-771.

Wang, L., Jacques, S.L., Zheng, L-Q., 1995. MCML - Monte Carlo modeling of photon transport in multi-layered tissues. Computer Methods and Programs in Biomedicine 47, 131-146.

Wolf, M., Ferrari, M., Quaresima, V., 2007. Progress of near-infrared spectroscopy and topography for brain and muscle clinical applications. J. Biomed. Opt. 12, 062104.

Wyatt, J.S., Cope, M., Delpy, D.T., van der Zee, P., Arridge, S., Edwards, A.D., Reynolds, E.O., 1990. Measurement of optical path length for cerebral near-infrared spectroscopy in newborn infants. Dev. Neurosci. 12, 140–144.

Formatted: Font: Not Bold, German (Germany)

Formatted: Font: Not Bold, German (Germany)

Formatted: Font: Not Bold, German (Germany)

Formatted: German (Germany)

Formatted: Font: Not Bold, German (Germany)

Yamashita, D., Yamanaka, T., Suzuki, T., Ohmae, E., Ueda, Y., Oda, M., Yamashita, Y., 2003. Development of multi-channel time resolved spectroscopy system and application of this system to measurement of brain function. Proc. Optics Japan: Symposium on Biomed. Opt., 3, pp. 72–73.

Yokose, N., Sakatani, K., Murata, Y., Awano, T., Igarashi, T., Nakamura, S., Hoshino, T., Katayama, Y., 2010. Bed-side monitoring of cerebral blood oxygenation and hemodynamics after aneurysmal subarachnoid hemorrhage by quantitative time-resolved near infrared spectroscopy. World Neurosurg 73:508-513.

Yucel, M.A., Huppert, T.J., Boas, D.A. and Gagnon, L., 2012. Calibrating the BOLD signal during a motor task using an extended fusion model incorporating DOT, BOLD and ASL data. Neuroimage 61(4), 1268-1276.

Zhao, Q., Spinelli, L., Bassi, A., Valentini, G., Contini, D., Torricelli, A., Cubeddu, R., Zaccanti, G., Martelli, F., Pifferi, A., 2011. Functional tomography using a time-gated ICCD camera. Biomedical Optics Express 2(3), 705-716.

Zhao, Q., Spinelli, L., Torricelli, A., Cubeddu, R., Pifferi A., 2010. Reconstruction in Diffuse Optical Tomography Using Genetic Algorithm. Conference Paper Biomedical Optics, Sunday Poster Session (BSuD), Miami, Florida, April 11, 2010.

Formatted: Font: Not Bold, Italian (Italy)

Formatted: Italian (Italy)

Formatted: Font: Not Bold, Italian (Italy)

Formatted: Font: Not Bold, Italian (Italy)

List of Figures

Figure 1. Principles of TD NIRS.
(a) The geometry of TD NIRS measurements in the reflectance mode. The region where photon paths are more likely to occur (the so called "banana shape") is also schematically depicted; (b) TD NIRS signals at different values of the source detector distance (ρ = 10-30 mm, in steps of 5 mm) for fixed absorption coefficient (μ_a = 0.001 mm^{-1}) and reduced scattering coefficient (μ_s' = 1.0 mm^{-1}); (c) TD NIRS signals at fixed source detector distance (ρ =30 mm) and fixed reduced scattering coefficient (μ_s' = 1.0 mm^{-1}) for different values of the absorption coefficient (μ_a = 0.005-0.025 mm^{-1} in steps of 0.005 mm^{-1}); (d) TD NIRS signals at fixed source detector distance (ρ =30 mm) and fixed absorption coefficient (μ_a = 0.001 mm^{-1}) for different values of the reduced scattering coefficient (μ_s' = 0.75-1.75 mm^{-1} in steps of 0.5 mm^{-1}).

Fig.2 Typical TD NIRS signal.
Experimental DTOF (red diamonds) and corresponding IRF (blue diamonds), measured by the system described in Contini et al. (2006). An example of a time window (delay = 2000 ps; width = 1000 ps) used in the time-gating semi-empirical approach is also shown.

Figure 3 Photos of TD fNIRS devices.
(a) The fOXY medical device developed at Politecnico di Milano, Milan Italy (Contini et al., 2006; Contini et al., 2009); (b) the brain imager developed at the Institute of Biocybernetics and Biomedical Engineering, Warsaw, Poland (Kacprzak et al., 2007); (c) the brain imager developed at Physikalisch-Technische Bundesanstalt, Berlin, Germany (Wabnitz et al., 2005; Wabnitz et al., 2010); (d) the MONSTIR2 developed at the Department of Medical Physics and Bioengineering, University College London, United Kingdom (Hebden et al., 2012a; Hebden et al., 2012b); (e) the TGI-2 imager developed at Massachusetts General Hospital, Athinoula A. Martinos Center, Charlestown, Massachusetts (Selb and Boas, 2012; Selb et al., 2013).

Figure 4. Sensitivity profiles in a homogeneous medium.
(a) Sensitivity profiles for TD reflectance in a homogeneous medium (μ_a = 0 mm^{-1}; and μ_s'= 1 mm^{-1}, n = 1.4) for different source detector distances ρ: (a) 2 mm; (b) 10 mm; (c) 20 mm; (d) 40 mm. Each line represents the contour edge of the contrast at 5% of the maximum, at a given time, from 500 to 4000 ps in steps of 500 ps. Source (red arrow) and detector (green arrow) positions are also shown. Simulations were performed with the analytical solution to the DE (Martelli et al., 2009).

Figure 5. Sensitivity maps in a head model for different source detector distances and time-gates.
(a) $\rho \cong 20$ mm, $t = 1000$ ps; (b) $\rho \cong 20$ mm, $t = 5000$ ps; (c) $\rho \cong 40$ mm, $t = 1000$ ps; (d) $\rho \cong 40$ mm, $t = 5000$ ps. Monte-Carlo forward simulations in a segmented volumetric 3D domain based on a digital head (Collins et al., 1998) have been calculated using 10^6 launched photons. We chose realistic optical properties for the brain structures (Boas et al., 2005). The photons have been simulated as leaving light sources positioned over C1, C3h and C3 positions of the 10/20 system. Sensitivity maps were then calculated via time convolution of forward solutions for pairs C3-C3h ($\rho \cong 20$ mm) and C3-C1 ($\rho \cong 40$ mm).

Figure 6. Penetration depth.
(a) Contrast as a function of depth of the perturbation for different time-gates (constant width: 500 ps, increasing delay: 500, 1500, 2500, and 3500 ps), and for the CW case (delay: 0 ps, width: 0-4500 ps,).;
(b) Contrast as a function of time (at the DTOF scale) for different depths of the perturbation.
Background medium: $\mu_a = 0.01$ mm^{-1}, $\mu_s' = 1.0$ mm^{-1}; $\rho = 30$ mm; perturbation: black PVC cylinder (volume = 500 mm^3) positioned at different depths in the mid plane between source and detector. The formula A1 was used for calculating the contrast.

Figure 7. Depth selectivity.
Contrast (left column) and estimated absorption changes (right column) in a two layered medium (upper layer thickness = 10 mm, lower layer thickness = 40 mm) for different time-gates (constant width: 500 ps, increasing delay: 500, 1000, 2000, and 4000 ps), and for the CW case (delay: 0 ps, width: 0-5000 ps,). Top row: absorption was changed only in the upper layer. Bottom row: absorption was changed only in the bottom layer. For both cases, but only for the latest time-gate (delay: 4000 ps, width: 500 ps) we have also applied the corrections A6 and A7 introduced by Selb et al. (2005) and Contini et al. (2007), indicated with "*" and "**", respectively.
Background medium: $\mu_a = 0.01$ mm^{-1}, $\mu_s' = 1.0$ mm^{-1}; $\rho = 30$ mm.

Figure 8: Contrast-to-noise ratio.
Contrast-to-noise ratio (CNR) as a function of depth, for different time gates (constant width: 500 ps, increasing delay: 500, 1500, 2500, and 3500 ps), and for the CW case (delay: 0 ps, width: 0-4500 ps,).;.
Background medium: $\mu_a = 0.01$ mm^{-1}, $\mu_s' = 1.0$ mm^{-1}; $\rho = 30$ mm; perturbation: black PVC cylinder (volume = 500 mm^3) positioned at different depths in the mid plane between source and detector. The formula A1 was used for the calculation of the contrast.

Figure 9. Finger tapping experiment.

Contrast at 690 nm (blue) and 830 nm (red) for different time-gates with constant width (250 ps) and increasing delay: (a) 0 ps, (b) 250 ps, (c) 500 ps, (d) 750 ps, (e) 1000 ps, (f) 1500 ps, (g) 2000 ps. Contrast for the moments of the DTOF: (h) 0^{th} order moment, (i) 1^{st} order moment, (j) 2^{nd} order moment.
Estimated changes in HHb (blue) and O_2Hb (red) as calculated from photons integrated in: (k) an early time window (delay: 0 ps, width: 500 ps, mean time-of-flight: 250 ps); (l) for the CW case (delay: 0 ps, width: 2500 ps); (m) a late time window (delay: 1750 ps, width: 750 ps, mean time-of-flight: 2125 ps); (n) late time window (delay: 1750 ps, width: 750 ps) with correction for changes in early time window (delay: 0 ps, width: 500 ps), formula A6; (o) same as (n), but formula A7.
Average and standard deviation over 10 repetitions are shown for all plotted parameters.
The black vertical lines and the green horizontal line mark the task period.

~~Contrast at 690 nm (blue) and 830 nm (red) for different time-gates with constant width (250 ps) and increasing delay: (a) 0 ps, (b) 250 ps, (c) 500 ps, (d) 750 ps, (e) 1000 ps, (f) 1250 ps, (g) 1500 ps, (h) 1750 ps, (i) 2000 ps. (j) contrast for the CW case (delay: 0 ps, width: 2500 ps).~~
~~Estimated changes in HHb (blue) and O_2Hb (red) as calculated from photons integrated in: (k) an early time window (delay: 0 ps, width: 500 ps, mean time-of-flight: 250 ps); (l) for the CW case (delay: 0 ps, width: 2500 ps); (m) a late time window (delay: 1750 ps, width: 750 ps, mean time-of-flight: 2125 ps); (n) late time window (delay: 1750 ps, width: 750 ps) with correction for changes in early time window (delay: 0 ps, width: 500 ps), formula A6; (o) same as (n), but formula A7.~~
~~Average with standard deviation over 10 repetitions are shown for all plotted parameters.~~
~~The black vertical lines and the green horizontal line mark the task period.~~

Figure 10. Valsalva maneuver experiment.

Contrast at 690 nm (blue) and 830 nm (red) for different time-gates with constant width (250 ps) and increasing delay: (a) 0 ps, (b) 250 ps, (c) 500 ps, (d) 750 ps, (e) 1000 ps, (f) 1500 ps, (g) 2000 ps. Contrast for the moments of the DTOF: (h) 0^{th} order moment, (i) 1^{st} order moment, (j) 2^{nd} order moment.
Estimated changes in HHb (blue) and O_2Hb (red) as calculated from photons integrated in: (k) an early time window (delay: 0 ps, width: 500 ps, mean time-of-flight: 250 ps); (l) for the CW case (delay: 0 ps, width: 2500 ps); (m) a late time window (delay: 1750 ps, width: 750 ps, mean time-of-flight: 2125 ps); (n) late time window (delay: 1750 ps, width: 750 ps) with correction for changes in early time window (delay: 0 ps, width: 500 ps), formula A6; (o) same as (n), but formula A7.
Average and standard deviation over 5 repetitions are shown for all plotted parameters.
The black vertical lines and the green horizontal line mark the task period.

Contrast at 690 nm (blue) and 830 nm (red) for different time-gates with constant width (250 ps) and increasing delay: (a) 0 ps, (b) 250 ps, (c) 500 ps, (d) 750 ps, (e) 1000 ps, (f) 1250 ps, (g) 1500 ps, (h) 1750 ps, (i) 2000 ps. (j) contrast for the CW case (delay: 0 ps, width: 2500 ps).

Estimated changes in HHb (blue) and O_2Hb (red) as calculated from photons integrated in: (k) an early time window (delay: 0 ps, width: 500 ps, mean time-of-flight: 250 ps); (l) for the CW case (delay: 0 ps, width: 2500 ps); (m) a late time window (delay: 1750 ps, width: 750 ps, mean time-of-flight: 2125 ps); (n) late time window (delay: 1750 ps, width: 750 ps) with correction for changes in early time window (delay: 0 ps, width: 500 ps), formula A6; (o) same as (n), but formula A7.

Average with standard deviation over 10 repetitions are shown for all plotted parameters.

The black vertical lines and the green horizontal line mark the task period.

Figure 1

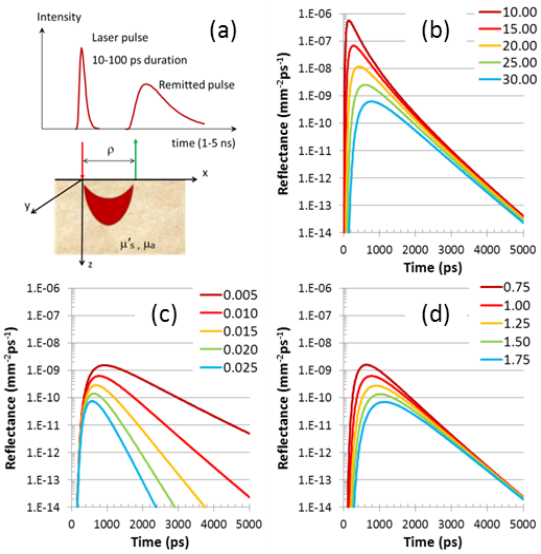

Figure 1. Principles of TD NIRS.

(a) The geometry of TD NIRS measurements in the reflectance mode. The region where photon paths are more likely to occur (the so called "banana shape") is also depicted; (b) TD NIRS signals at different values of the source detector distance (ρ = 10-30 mm, in steps of 5 mm) for fixed absorption coefficient (μ_a = 0.001 mm^{-1}) and reduced scattering coefficient (μ_s' = 1.0 mm^{-1}); (c) TD NIRS signals at fixed source detector distance (ρ =30 mm) and fixed reduced scattering coefficient (μ_s' = 1.0 mm^{-1}) for different values of the absorption coefficient (μ_a = 0.005-0.025 mm^{-1} in steps of 0.005 mm^{-1}); (d) TD NIRS signals at fixed source detector distance (ρ =30 mm) and fixed absorption coefficient (μ_a = 0.001 mm^{-1}) for different values of the reduced scattering coefficient (μ_s' = 0.75-1.75 mm^{-1} in steps of 0.5 mm^{-1}).

Figure 2

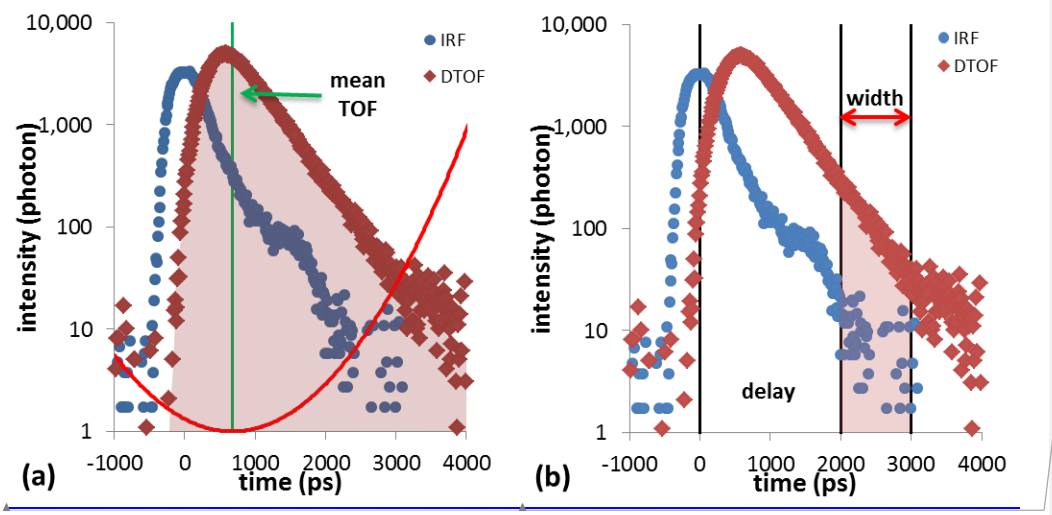

Formatted: Font: Times New Roman

Formatted: Font: Times New Roman

Fig.2 Typical TD NIRS signal.

Experimental DTOF (red diamonds) and corresponding IRF (blue diamonds), measured by the system described in Contini et al. (2006). In panel (a) they are also shown the zero-order moment (total photons, shaded area), the first-order moment (mean TOF, green line) and the time weight function of the second-order moment (variance, red line) for the DTOF. In panel (b) an example of time window (delay = 2000 ps, width = 1000 ps, shaded area) used in the time-gating semi-empirical approach is shown for the same DTOF.

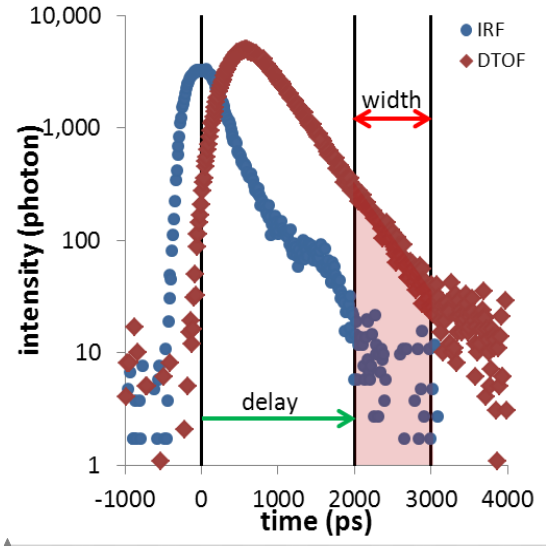

Formatted: Font: Times New Roman

~~Fig.2 Typical TD-NIRS signal.~~

~~Experimental DTOF (red diamonds) and corresponding IRF (blue diamonds), measured by the system described in Contini et al. (2006). An example of a time window (delay = 2000 ps; width = 1000 ps) used in the time-gating semi-empirical approach is also shown.~~

Figure 3

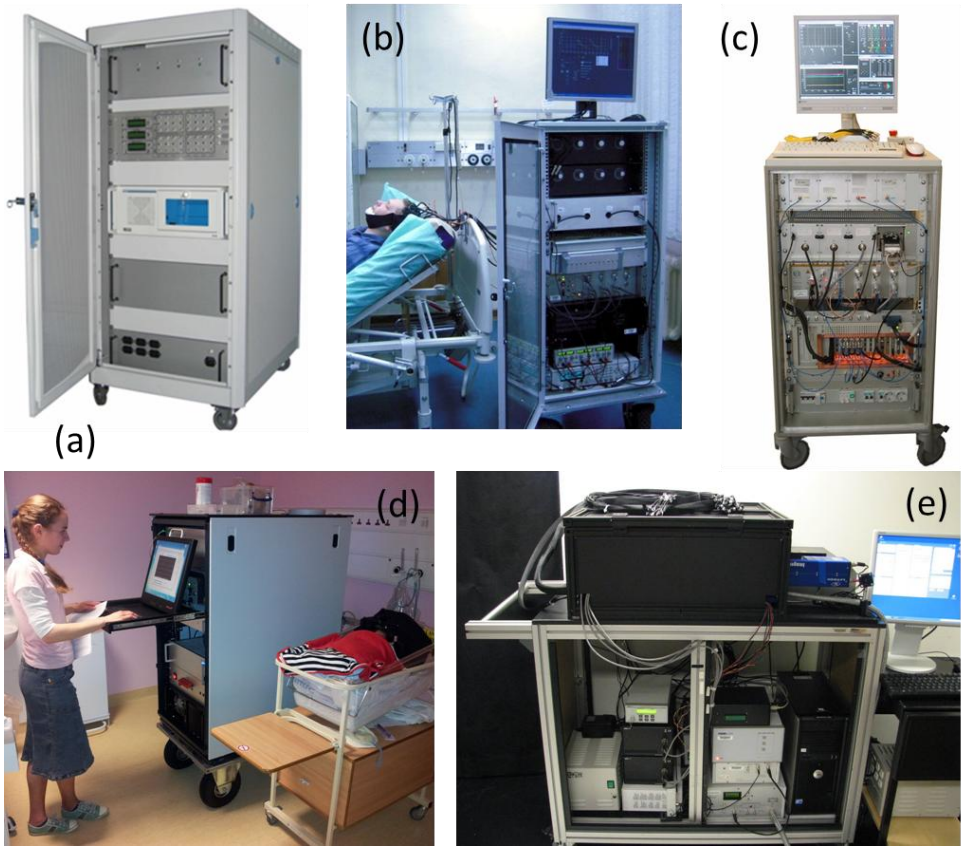

Figure 3 Photos of TD fNIRS devices.

(a) The fOXY medical device developed at Politecnico di Milano, Milan Italy (Contini et al., 2006; Contini et al., 2009); (b) the brain imager developed at the Institute of Biocybernetics and Biomedical Engineering, Warsaw, Poland (Kacprzak et al., 2007); (c) the brain imager developed at Physikalisch-Technische Bundesanstalt, Berlin, Germany (Wabnitz et al., 2005; Wabnitz et al., 2010); (d) the MONSTIR2 developed at the Department of Medical Physics and Bioengineering, University College London, United Kingdom (Hebden et al., 2012a; Hebden et al., 2012b); (e) the TGI-2 imager developed at Massachusetts General Hospital, Athinoula A. Martinos Center, Charlestown, Massachusetts (Selb and Boas, 2012; Selb et al., 2013).

Figure 4

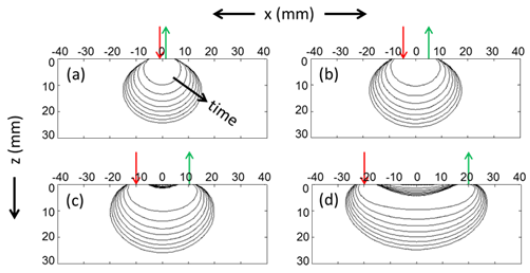

Figure 4. Sensitivity profiles in a homogeneous medium.

(a) Sensitivity profiles for TD reflectance in a homogeneous medium (μ_a = 0 mm^{-1}; and μ_s'= 1 mm^{-1}, n = 1.4) for different source detector distances ρ: (a) 2 mm; (b) 10 mm; (c) 20 mm; (d) 40 mm. Each line represents the contour edge of the contrast at 5% of the maximum, at a given time, from 500 to 4000 ps in steps of 500 ps. Source (red arrow) and detector (green arrow) positions are also shown. Simulations were performed with the analytical solution to the DE (Martelli et al., 2009).

Figure 5

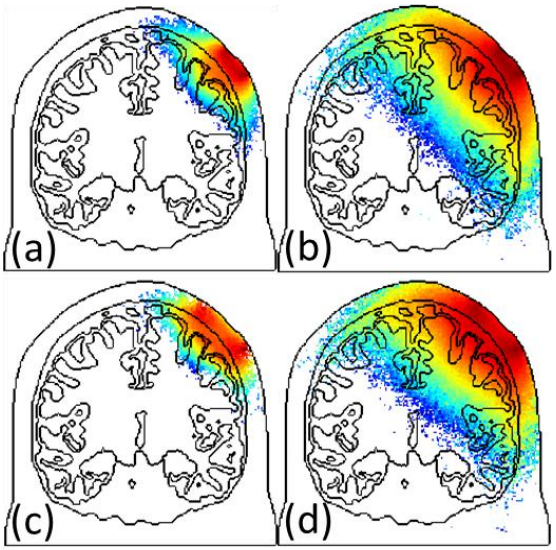

Figure 5. Sensitivity maps in a head model for different source detector distances and time-gates. (a) $\rho \cong 20$ mm, $t = 1000$ ps; (b) $\rho \cong 20$ mm, $t = 5000$ ps; (c) $\rho \cong 40$ mm, $t = 1000$ ps; (d) $\rho \cong 40$ mm, $t = 5000$ ps. Monte-Carlo forward simulations in a segmented volumetric 3D domain based on a digital head (Collins et al., 1998) have been calculated using 10^6 launched photons. We chose realistic optical properties for the brain structures (Boas et al., 2005). The photons have been simulated as leaving light sources positioned over C1, C3h and C3 positions of the 10/20 system. Sensitivity maps were then calculated via time convolution of forward solutions for pairs C3-C3h ($\rho \cong 20$ mm) and C3-C1 ($\rho \cong 40$ mm).

Figure 6

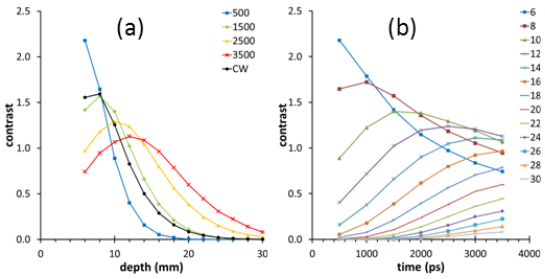

Figure 6. Penetration depth.

(a) Contrast as a function of depth of the perturbation for different time-gates (constant width: 500 ps, increasing delay: 500, 1500, 2500, and 3500 ps), and for the CW case (delay: 0 ps, width: 0-4500 ps,).; (b) Contrast as a function of time (at the DTOF scale) for different depths of the perturbation. Background medium: μ_a = 0.01 mm^{-1}, μ_s' = 1.0 mm^{-1}; ρ = 30 mm; perturbation: black PVC cylinder (volume = 500 mm^3) positioned at different depths in the mid plane between source and detector. The formula A1 was used for calculating the contrast.

Figure 7

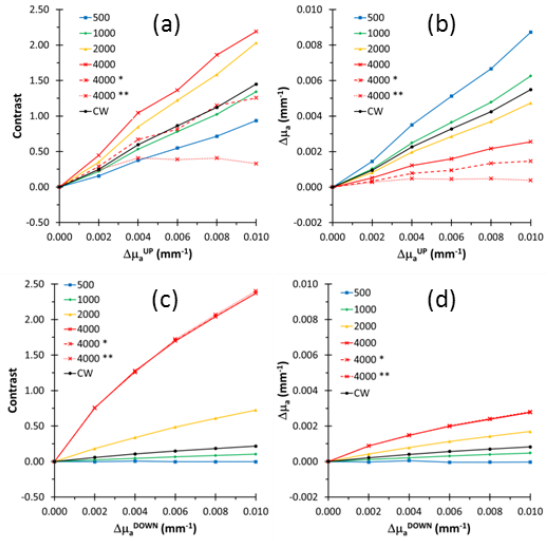

Figure 7. Depth selectivity.

Contrast (left column) and estimated absorption changes (right column) in a two layered medium (upper layer thickness = 10 mm, lower layer thickness = 40 mm) for different time-gates (constant width: 500 ps, increasing delay: 500, 1000, 2000, and 4000 ps), and for the CW case (delay: 0 ps, width: 0-5000 ps,). Top row: absorption was changed only in the upper layer. Bottom row: absorption was changed only in the bottom layer. For both cases, but only for the latest time-gate (delay: 4000 ps, width: 500 ps) we have also applied the corrections A6 and A7 introduced by Selb et al. (2005) and Contini et al. (2007), indicated with "*" and "**", respectively.

Background medium: μ_a = 0.01 mm^{-1}, μ_s' = 1.0 mm^{-1}; ρ = 30 mm.

Figure 8

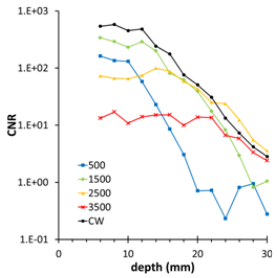

Figure 8: Contrast-to-noise ratio.

Contrast-to-noise ratio (CNR) as a function of depth, for different time gates (constant width: 500 ps, increasing delay: 500, 1500, 2500, and 3500 ps), and for the CW case (delay: 0 ps, width: 0-4500 ps,).;. Background medium: μ_a = 0.01 mm^{-1}, μ_s' = 1.0 mm^{-1}; ρ = 30 mm; perturbation: black PVC cylinder (volume = 500 mm^3) positioned at different depths in the mid plane between source and detector. The formula A1 was used for the calculation of the contrast.

Figure 9

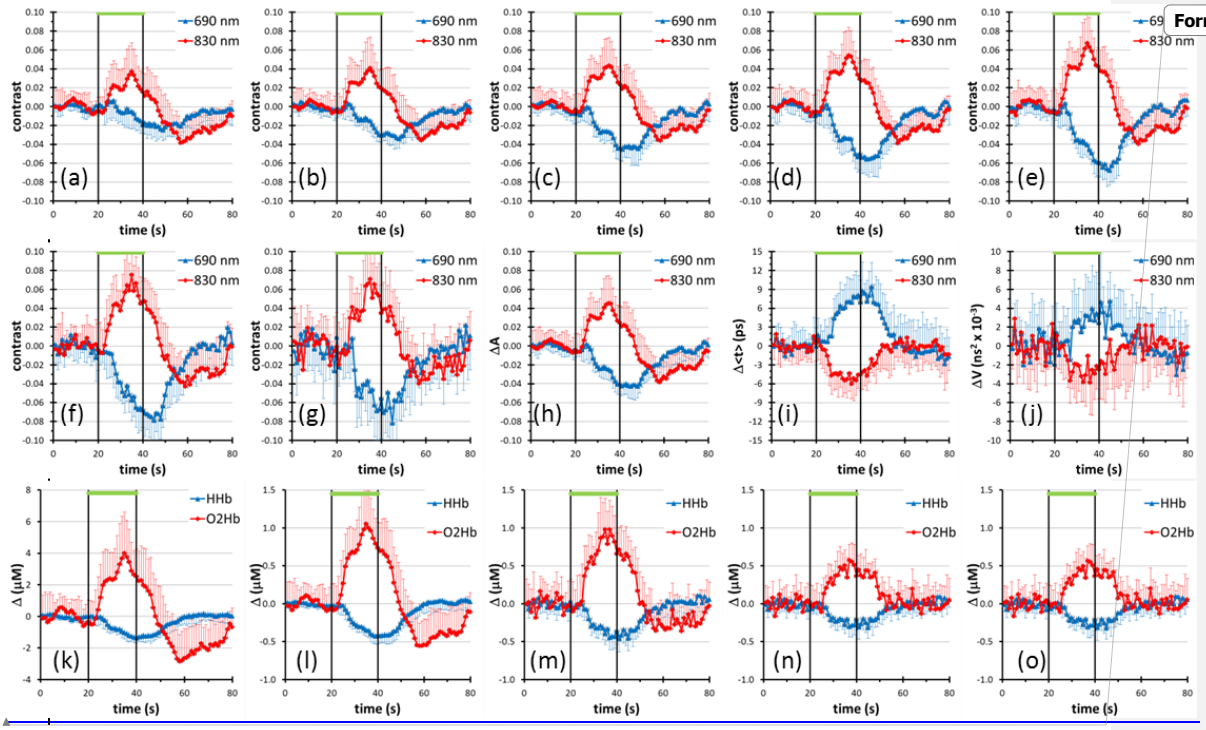

Formatted: Font: Times New Roman

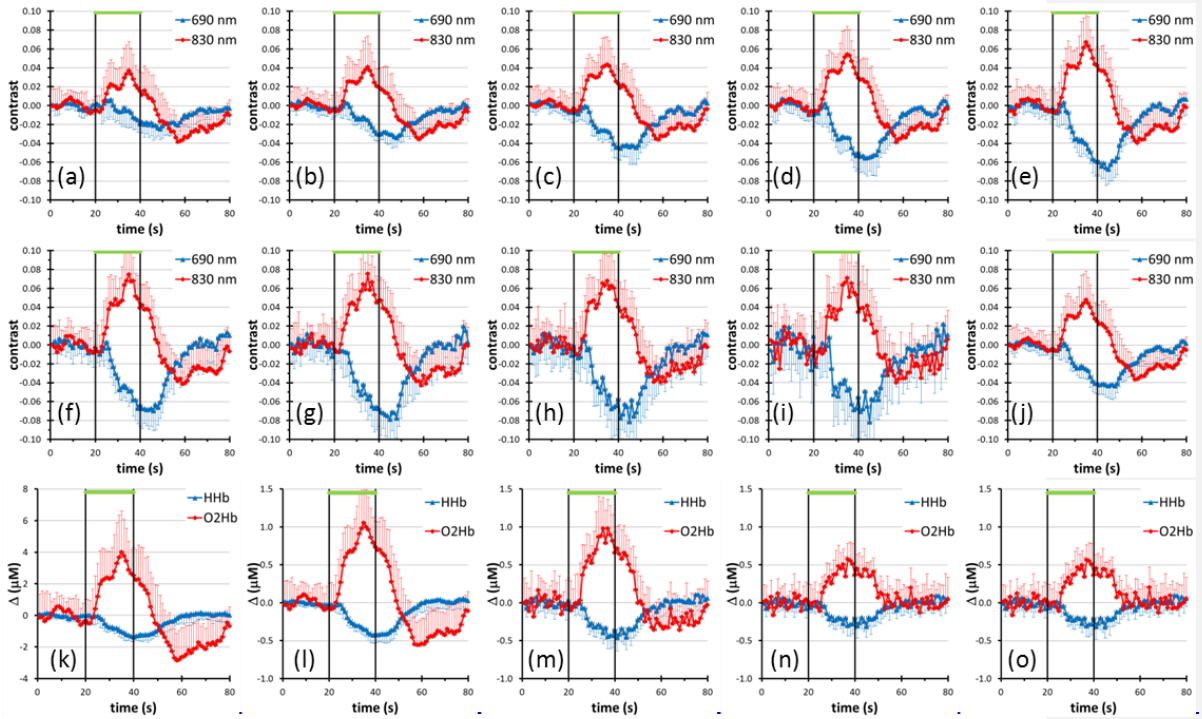

Figure 9. Finger tapping experiment.

Contrast at 690 nm (blue) and 830 nm (red) for different time-gates with constant width (250 ps) and increasing delay: (a) 0 ps, (b) 250 ps, (c) 500 ps, (d) 750 ps, (e) 1000 ps, (f) 1500~~250~~ ps, (g) 2000~~1500~~ ps. Contrast for the moments of the DTOF:~~,~~ (h) 0th order ~~1750 ps~~moment~~,~~, (i) ~~2000 ps~~1st order moment~~,~~ (j) 2nd order moment~~contrast for the CW case (delay: 0 ps, width: 2500 ps)~~.

Estimated changes in HHb (blue) and O_2Hb (red) as calculated from photons integrated in: (k) an early time window (delay: 0 ps, width: 500 ps, mean time-of-flight: 250 ps); (l) for the CW case (delay: 0 ps, width: 2500 ps); (m) a late time window (delay: 1750 ps, width: 750 ps, mean time-of-flight: 2125 ps); (n) late time window (delay: 1750 ps, width: 750 ps) with correction for changes in early time window (delay: 0 ps, width: 500 ps), formula A6; (o) same as (n), but formula A7.

Average ~~with~~ and standard deviation over 10 repetitions are shown for all plotted parameters.

The black vertical lines and the green horizontal line mark the task period.

Formatted: Superscript

Formatted: Superscript

Formatted: Superscript

Figure 10

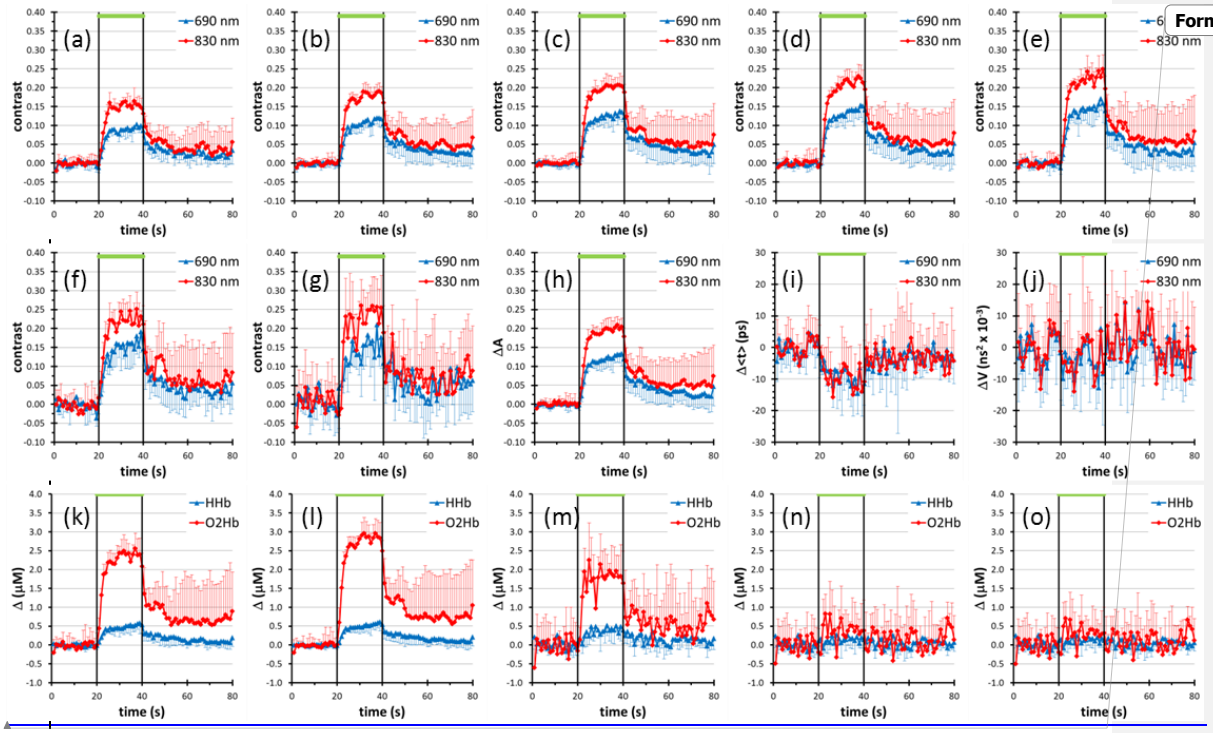

Formatted: Font: Times New Roman

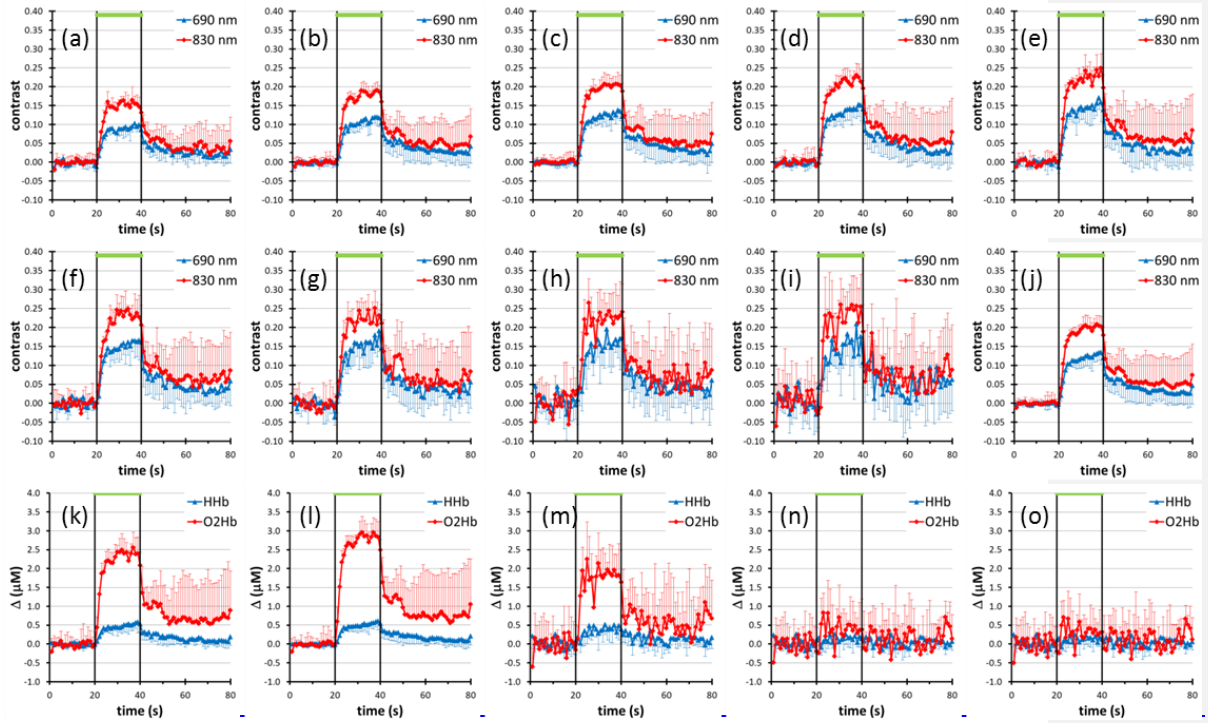

Figure 10. Valsalva maneuver experiment.

Contrast at 690 nm (blue) and 830 nm (red) for different time-gates with constant width (250 ps) and increasing delay: (a) 0 ps, (b) 250 ps, (c) 500 ps, (d) 750 ps, (e) 1000 ps, (f) 1500 ps, (g) 2000 ps. Contrast for the moments of the DTOF: (h) 0^{th} order moment, (i) 1^{st} order moment, (j) 2^{nd} order moment.

~~Contrast at 690 nm (blue) and 830 nm (red) for different time-gates with constant width (250 ps) and increasing delay: (a) 0 ps, (b) 250 ps, (c) 500 ps, (d) 750 ps, (e) 1000 ps, (f) 1250 ps, (g) 1500 ps, (h) 1750 ps, (i) 2000 ps. (j) contrast for the CW case (delay: 0 ps, width: 2500 ps).~~

Estimated changes in HHb (blue) and O_2Hb (red) as calculated from photons integrated in: (k) an early time window (delay: 0 ps, width: 500 ps, mean time-of-flight: 250 ps); (l) for the CW case (delay: 0 ps, width: 2500 ps); (m) a late time window (delay: 1750 ps, width: 750 ps, mean time-of-flight: 2125 ps); (n) late time window (delay: 1750 ps, width: 750 ps) with correction for changes in early time window (delay: 0 ps, width: 500 ps), formula A6; (o) same as (n), but formula A7.

Average ~~with~~ and standard deviation over ~~10~~ 5 repetitions are shown for all plotted parameters.

The black vertical lines and the green horizontal line mark the task period.

List of Tables

Table 1. Traditional TD fNIRS systems

Group	Light source	Wavelength (nm)	Average power (mW)	Repetition rate (MHz)	Detection technique	Count rate (MHz)	IRF FWHM (ps)	Source channels	Detection channels	Reference
Physikalisch-Technische Bundesanstalt Berlin, Germany	Ti:Sapphire	775, 805, 835 (serial)	800 (?)	80 (?)	TCSPC	NA	35	1	1	Obrig et al., 1996
Standford University Palo Alto, California	Laser diode	785, 850	0.1	NA	OTDR	NA	NA	34 (serial)	34	Hintz et al., 1998
Shimadzu Corporation, Hamamatsu Photonics, Ministry of Int. Trade and Industry, Hokkaido University Japan	Laser diode	761, 791, 830	0.25	5	TCSPC	1	150		64	Eda et al., 1999
Politecnico di Milano Milan, Italy	Laser diode	672, 818	1	80	TCSPC	1	200	4	4	Cubeddu et al., 1999
University of Pennsylvania, Philadelphia, Pennsylvania	Laser diode	780, 830	0.020	5	TCSPC	4	50	9	8	Ntziachristos et al., 1999
TRS-10, Hamamatsu Photonics Japan	Laser diode	759, 797, 833	<0.1	5	TCSPC	<1	150	1	1	Oda et al., 1999 Ohmae et al., 2007
University College London London, United Kingdom	Ti:Sapphire / fiber laser	800 780, 815	800 >50	80 40	TCSPC	0.3	80-150	32 (serial)	32	Schmidt et al., 2000 Gibson et al, 2006
TRS-16, Hamamatsu Photonics Japan	Laser diode	760, 800, 830	1	5	TCSPC	<4	500	8 (serial)	16	Yamashita et al., 2003
Physikalisch-Technische Bundesanstalt Berlin, Germany	Laser diode	687, 803, 826	0.5	20	TCSPC	1	600	1	4	Liebert et al., 2004
Politecnico di Milano Milan, Italy	Laser diode	685, 780	1	80	TCSPC	4	200	2	8	Torricelli et al., 2004
Institut de Physique Biologique Strasbourg, France	Laser diode	690, 785, 830, 870	1	20	TCSPC	8	200	1	8	Montcel et al., 2004 Montcel et al., 2005
Martinos Center for Biomedical Imaging, Boston,	Ti:Sapphire	One wavelength tuned in range 750 to 850 nm	1000	80	Time-gated ICCD	NA	500	32 (serial)	18	Selb et al., 2005 Selb et al., 2006

Table 2. State-of-the-art TD fNIRS systems

Group	Light source	Wavelength (nm)	Average power (mW)	Repetition rate (MHz)	Detection technique	Count rate (MHz)	IRF FWHM (ps)	Source channels	Detection channels	Reference
TRS-20, Hamamatsu Photonics Japan	Laser diode	760, 800, 830	0.25	5	TCSPC	1	250	2	2	Oda et al., 2009
Physikalisch-Technische Bundesanstalt Berlin, Germany	Laser diode	689, 797, 828	1	42	TCSPC	2	750	9 (serial)	4	Wabnitz et al., 2005 Wabnitz et al., 2010
Politecnico di Milano Milan, Italy	Laser diode	690, 830	1	80	TCSPC	8	500	16 (serial)	16	Contini et al., 2006 Contini et al., 2009
Politecnico di Milano Milan, Italy	Laser diode	690, 830	1	80	TCSPC	~~48~~	500	2	2	Re et al., 2010
Institute of Biocybernetics and Biomedical Engineering, Warsaw, Poland	Laser diode	687, 832	1	80	TCSPC	16	<800	18 (serial)	8	Kacprzak et al., 2007

Formatted: Font: Not Bold (Germany)
Formatted: Font: Not Bold (France)
Formatted: French (France)
Formatted: German (Germany)
Formatted: Font: Not Bold (France)
Formatted: French (France)
Formatted: Font: Not Bold (Germany)
Formatted: German (Germany)
Formatted: Font: Not Bold (Italy)
Formatted: Italian (Italy)
Formatted: Italian (Italy)
Formatted: Font: Not Bold (Italy)
Formatted: Italian (Italy)
Formatted: Font: Not Bold (Italy)
Formatted: Italian (Italy)
Formatted: Font: Not Bold (Italy)
Formatted: Italian (Italy)

Table 3. Next generation TD fNIRS systems

Group	Light source	Wavelength (nm)	Average power (mW)	Repetition rate (MHz)	Detection technique	Count rate (MHz)	IRF FWHM (ps)	Source channels	Detection channels	Reference
University College London London, United Kingdom MONSTIR2	SC fiber laser	Up to8 selected in the 650-825 nm spectral range	<2.5	40	TCSPC	8	220	32 (serial)	32	Hebden et al., 2012a Hebden et al., 2012b
Martinos Center for Biomedical Imaging, Boston TGI2	SC fiber laser	Up to6 selected in the 680-840 nm spectral range	<100	~~40~~60	Time-gated ICCD	NA	500	~~32~~16 (serial)	~~18~~25	Selb and Boas, 2012 Selb et al., 2013
Politecnico di Milano Milan, Italy fOXY2	Laser diode	690, 830	1	80	TCSPC	16	400	16 (serial)	8	Contini et al., 2013b
Physikalisch-Technische Bundesanstalt Berlin, Germany	Laser diode	705, 830	<5	40	TCSPC	2	750	10	4	Steinkellner et al., 2012
Physikalisch-Technische Bundesanstalt Berlin, Germany Confocal null distance	SC fiber laser	690	1	20	TCSPC	2	<100	1 (scanning)	1 (scanning)	Mazurenka et al., 2012 Mazurenka et al., 2013
Politecnico di Milano Milan, Italy Null distance	SC fiber laser	710, 820	<100	40	TCSPC Fast gated	2	100	1	1	Contini et al., 2013a
Ecole Polytechnique Federale de Lausanne and University Hospital Zurich 3D SPAD imager	Laser diode	780	<3	50	TCSPC (TDC)	16	<300	2 (scanning)	32x32	Mata Pavia et al., 2011a; Mata Pavia et al., 2011b